Tectonophysics 580 (2012) 1–26

Contents lists available at SciVerse ScienceDirect

Tectonophysics

journal homepage: www.elsevier.com/locate/tecto

Review Article

Crustal stress determination from boreholes and rock cores: Fundamental principles

Douglas R. Schmitt *, Claire A. Currie, Lei Zhang

Institute for Geophysical Research, CCIS 4-138, Dept. of Physics, University of Alberta, Edmonton, Alberta, Canada T6G 2E1

ARTICLE INFO

Article history:
Received 5 January 2012
Received in revised form 5 August 2012
Accepted 21 August 2012
Available online 4 September 2012

Keywords:
Stress measurement
Hydraulic fracture
Core fracture
Acoustic logging
Borehole breakout
Borehole fractures

ABSTRACT

Obtaining quantitative information on the state of stress in the crust can only be accomplished by accessing the zone of interest by drilling. The borehole cavity, however, disrupts the virgin stress state by concentrating stresses in predictable patterns with a number of consequences. At sufficiently low stress magnitudes, the concentrated stresses amplify the elastic anisotropy azimuthally around the borehole because the elastic properties of most rocks depend nonlinearly on stress. At higher levels, the stresses damage then fracture the rock near the wellbore wall or within a growing core stub. Indeed, almost all of the borehole techniques indirectly measure stress through these manifestations of the concentrated stresses. This contribution reviews, at a fundamental level, the concentration of stresses by the borehole, the effects on the materials in the borehole's vicinity, and how these are used to infer stress states. Stress concentrations applied to rocks, which are generally nonlinear elastic materials, induce both radial and azimuthal variations in elastic wave speeds near the borehole that can be used to infer stress directions from advanced acoustic logging methods. Hydraulic fractures initiate, propagate, and remain propped open by measured pressures that can be interpreted with knowledge of the stress concentrations to obtain quantitative stress magnitudes. At higher stress levels, the rock fails producing borehole breakouts or drilling induced tensile fractures both of which are indicative of stress directions and can be used to constrain stress magnitudes. Similarly, the various styles of drilling induced core fractures indicate both stress directions and the faulting environment encountered. Unfortunately, no method currently allows for complete determination of the stress tensor; using a number of different but complementary techniques is necessary to best constrain in situ stress states.

Contents

* Corresponding author. Tel.: +1 780 492 3985; fax: +1 780 492 0714.
E-mail address: dschmitt@ualberta.ca (D.R. Schmitt).

0040-1951/$ – see front matter © 2012 Elsevier B.V. All rights reserved.
http://dx.doi.org/10.1016/j.tecto.2012.08.029

1. Introduction

Crustal stresses are generated by gravitational loading, thermal excursions, pore fluid diffusion, elevation differences, and, of course, tectonic deformation. As such, crustal stress can tell us a great deal about dynamic processes within the Earth particularly with regards to plate tectonics where to a large degree we still do not fully understand what exactly drives or impedes plate motions and fault movements. Stress states lead to the ultimate failure of rock at many scales ranging from the largest earthquakes to the smallest micro-seismic events; having better knowledge of stress states is crucial to understanding such seismicity. Knowledge of in situ stress states has practical implications with regards to the stability and safety of underground workings and boreholes, and the capacity to carry out hydraulic stimulations for water or hydrocarbon recovery. With the rapid rise of enhanced recovery from low permeability 'tight' sands and shale by hydraulic fracturing methods, the interest in understanding and detecting stress states has grown rapidly in recent years.

Quantitatively measuring or constraining stresses deep in the Earth remains elusive. There are currently a number of different borehole methodologies available to researchers; the purpose of this contribution is to overview these from a fundamental perspective. In order that the reader understands in each case the basic physics of the problem we ignore the crucial influence of pore pressure on many of these techniques. Many will see this as an oversight, but including effective pressure concepts at the outset can obscure the underlying principles. Further, the literature is replete with cases in which the concept of effective pressure is not correctly applied and ignoring pore pressure in this contribution eliminates the need to deal with such issues at this time. Regardless, the reader can find this information cited in the supporting literature. The reader can begin with a number of textbooks describing stress measurement methods (e.g., Amadei and Stephannson, 1997; Fjaer et al., 2008; Jaeger et al., 2007; Zang and Stephannson, 2010; Zoback, 2007).

This contribution focuses on methods from deeper boreholes. That said, mapping of igneous dyke directions (e.g., Grasso et al., 1991; Gudmundsson, 2006) and caldera ellipticity (Paulsen and Wilson, 2007; Ruch and Walter, 2010), earthquake focal mechanisms, near surface quarry floor buckling (Adams, 1982), and blasting induced axial fractures (Pascal et al., 2010) or blast hole offsets (Bell, 1985) can all be used to provide stress direction information. An entire other class of stress-relief measurements from shallow boreholes are also not discussed here despite their importance in underground construction. These include various techniques to measure the stress relief deformation near a slot cut into a stressed rock mass (Corthesy et al., 1999), various 'overcoring' methods (Leite et al., 2010), and laser interferometric based hole drilling techniques (Schmitt et al., 2006).

The contribution begins with some background information in order to set the definitions and framework upon which the review focuses. This is followed by a discussion on the dependence of the physical properties of rocks on stress, a factor usually ignored but which actually provides the basis for some of the stress determination techniques. With this background in place, both qualitative and quantitative stress measurement methods are presented. The paper concludes with some thoughts on future directions in stress determination.

1.1. Basic theory

The literature on elasticity theory is vast with numerous textbooks at a variety of levels readily available, and only a small overview is necessary here to set the definitions. First, at a given point in the solid Earth and relative to an arbitrary reference frame, the stresses, or normalized forces in units of Pascals (1 Pa = N/m^2) are distributed around an infinitesimal cube as shown in Fig. 1. Two types of stresses are noted: those whose tractions will be perpendicular to the face of the cube and called normal stresses and denoted with a σ symbol, and those whose tractions are parallel to the surface called shear stresses and denoted using a τ symbol. As illustrated in Fig. 1a, the first subscript indicates the normal of the plane upon which the given stress acts and the second indicates the direction of the associated traction.

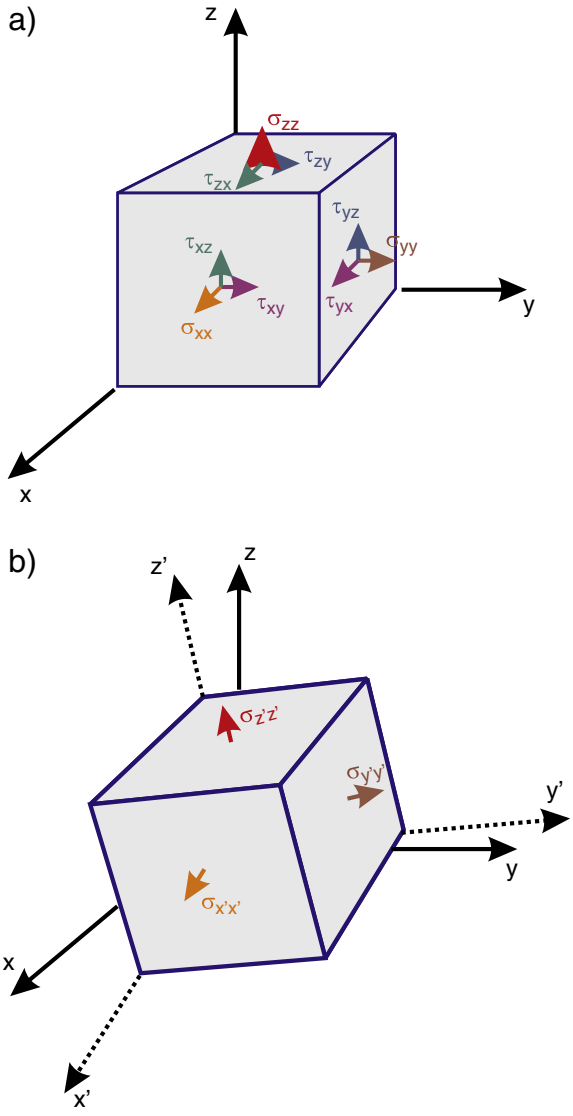

Fig. 1. a) Complete stress state on infinitesimal cube of solid material in arbitrary x–y–z co-ordinate system with σ and τ representing normal and shear stresses, respectively. b) Rotation of the arbitrary co-ordinate frame x–y–z into the principal co-ordinate frame x'–y'–z' within which all the shear stresses vanish leaving only the three principal normal stresses. Stress sign convention shown with tensile normal stresses of negative sign as usually employed in the Geosciences and Geotechnical Engineering.

The six values apparent in Fig. 1 define a stress tensor σ that may be written in matrix format as

$$\sigma = \begin{bmatrix} \sigma_{xx} & \tau_{xy} & \tau_{xz} \\ \tau_{yx} & \sigma_{yy} & \tau_{yz} \\ \tau_{zx} & \tau_{zy} & \sigma_{zz} \end{bmatrix}. \quad (1)$$

It needs to be noted that this is a symmetric matrix with, for example, $\tau_{yx} = \tau_{xy}$. This is a 2nd order stress tensor. As such the values of components of the stress tensor will change if the co-ordinate frame is rotated although the invariants of the tensor do not. This is understood by analogy with a first order tensor (i.e. a vector) with three components the values of which change depending again upon the co-ordinate. The transformation is effected by

$$\sigma' = A\sigma A^T \quad (2)$$

where the rotation matrix A

$$A = \begin{bmatrix} a_{xx'} & a_{xy'} & a_{xz'} \\ a_{y'x} & a_{yy'} & a_{yz'} \\ a_{z'x} & a_{z'y} & a_{zz'} \end{bmatrix} \quad (3)$$

is composed of the direction cosines a_{ij} between the original x–y–z and new x'–y'–z' co-ordinate frames.

Consequently, one may find a principal co-ordinate frame x'–y'–z' where all of the shear stresses vanish leaving only the three principal normal stresses with the rotated tensor appearing as

$$\sigma' = \begin{bmatrix} \sigma_{x'x'} & 0 & 0 \\ 0 & \sigma_{y'y'} & 0 \\ 0 & 0 & \sigma_{z'z'} \end{bmatrix} \quad (4)$$

and illustrated in Fig. 1b. While there appears to be only three components in σ', it must be remembered that the directions of these stresses are known. This requires knowledge of three angles, and such that six independent values are necessary to define the stress tensor regardless of co-ordinate frame.

A change in the stress state results in changes in both the volume and shape of an object. Briefly, a hypothetical fiber running through the material will undergo a change in length as the object deforms; this is referred to as a normal strain. A shear strain describes changes in the angles between two originally perpendicular fibers. For small strains, the strain tensor ε is

$$\varepsilon(x,y,z) = \begin{bmatrix} \varepsilon_{xx} & \varepsilon_{xy} & \varepsilon_{xz} \\ \varepsilon_{yx} & \varepsilon_{yy} & \varepsilon_{yz} \\ \varepsilon_{zx} & \varepsilon_{zy} & \varepsilon_{zz} \end{bmatrix} = \begin{bmatrix} \dfrac{\partial u_x}{\partial x} & \dfrac{1}{2}\left(\dfrac{\partial u_x}{\partial y} + \dfrac{\partial u_y}{\partial x}\right) & \dfrac{1}{2}\left(\dfrac{\partial u_x}{\partial z} + \dfrac{\partial u_z}{\partial x}\right) \\ \dfrac{1}{2}\left(\dfrac{\partial u_y}{\partial x} + \dfrac{\partial u_x}{\partial y}\right) & \dfrac{\partial u_y}{\partial y} & \dfrac{1}{2}\left(\dfrac{\partial u_y}{\partial z} + \dfrac{\partial u_z}{\partial y}\right) \\ \dfrac{1}{2}\left(\dfrac{\partial u_z}{\partial x} + \dfrac{\partial u_x}{\partial z}\right) & \dfrac{1}{2}\left(\dfrac{\partial u_z}{\partial y} + \dfrac{\partial u_y}{\partial z}\right) & \dfrac{\partial u_z}{\partial z} \end{bmatrix} \quad (5)$$

where the displacement vector $u(x,y,z)$ has the three components [u_x, u_y, u_z]. A principal strain tensor, too, may be found and in an isotropic material this will align with the principal stresses. This strain tensor is symmetric. The reader should take care to note that the 'engineering strain' is also often employed with, for illustration, $\gamma_{xy} = 2\varepsilon_{xy}$ for shear strains and $\gamma_{xx} = \varepsilon_{xx}$ for the normal strains. The advantage of engineering strains is that their value is that of the actual deformation that for shear strains is a small angle.

For the conditions of isotropic linear elasticity, the stresses and strains are related to one another via Hooke's Law, which may be written in a convenient Voigt matrix form as

$$\begin{bmatrix} \varepsilon_{xx} \\ \varepsilon_{yy} \\ \varepsilon_{zz} \\ 2\varepsilon_{yz} \\ 2\varepsilon_{zx} \\ 2\varepsilon_{xy} \end{bmatrix} = \begin{bmatrix} \gamma_{xx} \\ \gamma_{yy} \\ \gamma_{zz} \\ \gamma_{yz} \\ \gamma_{zx} \\ \gamma_{xy} \end{bmatrix} = \frac{1}{E}\begin{bmatrix} 1 & -\nu & -\nu & 0 & 0 & 0 \\ -\nu & 1 & -\nu & 0 & 0 & 0 \\ -\nu & -\nu & 1 & 0 & 0 & 0 \\ 0 & 0 & 0 & 2(1+\nu) & 0 & 0 \\ 0 & 0 & 0 & 0 & 2(1+\nu) & 0 \\ 0 & 0 & 0 & 0 & 0 & 2(1+\nu) \end{bmatrix}\begin{bmatrix} \sigma_{xx} \\ \sigma_{yy} \\ \sigma_{zz} \\ \tau_{yz} \\ \tau_{zx} \\ \tau_{xy} \end{bmatrix}. \quad (6)$$

Only two constants appear in the above equation. The first is the modulus of elasticity or Young's modulus E, and the second is Poisson's ratio ν. These are the only elastic parameters that are needed to define the stress–strain behavior of an isotropic linearly elastic material and they can readily be converted to the other isotropic elastic moduli of the bulk and shear moduli and the Lamé parameters if necessary. However, rocks are more generally anisotropic particularly, as will be discussed below, under deviatoric states of stress. The more anisotropic the material the larger the number of elastic constants required to define it such that the most general form of Hooke's law is:

$$\begin{bmatrix} \varepsilon_{xx} \\ \varepsilon_{yy} \\ \varepsilon_{zz} \\ 2\varepsilon_{yz} \\ 2\varepsilon_{zx} \\ 2\varepsilon_{xy} \end{bmatrix} = \begin{bmatrix} \varepsilon_{xx} \\ \varepsilon_{yy} \\ \varepsilon_{zz} \\ \gamma_{yz} \\ \gamma_{zx} \\ \gamma_{xy} \end{bmatrix} = \begin{bmatrix} S_{11} & S_{12} & S_{13} & S_{14} & S_{15} & S_{16} \\ S_{21} & S_{22} & S_{23} & S_{24} & S_{25} & S_{26} \\ S_{31} & S_{32} & S_{33} & S_{34} & S_{35} & S_{36} \\ S_{41} & S_{42} & S_{43} & S_{44} & S_{45} & S_{46} \\ S_{51} & S_{52} & S_{53} & S_{54} & S_{55} & S_{56} \\ S_{61} & S_{62} & S_{63} & S_{64} & S_{65} & S_{66} \end{bmatrix}\begin{bmatrix} \sigma_{xx} \\ \sigma_{yy} \\ \sigma_{zz} \\ \tau_{yz} \\ \tau_{zx} \\ \tau_{xy} \end{bmatrix} \quad (7)$$

where the S_{ij} represent the 21 independent (i.e., $S_{ij} = S_{ji}$) elastic compliances.

1.2. Crustal stress states

When working with stresses in the Earth we often assume that the direction of one of the principal stresses is vertical because the surface is essentially a free boundary and because the stress generating acceleration of gravity g is directed downwards. Under this paradigm, this principal stress is here denoted as S_V will be expected to have a depth h and density ρ dependent magnitude

$$S_V(h) = -\int_0^h \rho(h) g dh \quad (8)$$

where again the negative value arises due to the selection of the stress sign convention under the assumption that both g and h are positive numbers with the compression increasing with depth. By default, the other two principal stresses in the Earth must be directed horizontally and here we will denote them as S_H and S_h to indicate the greatest and least horizontal principal compressions, respectively. S_V may be estimated relatively easily if appropriate knowledge of the density overlying the point in question is known. The two horizontal stresses are not so readily found as they result from combinations of tectonic forces (e.g., Bott, 1993; Zoback et al., 1989) and crustal structure (e.g., McCutchen, 1982), surface topography (e.g., Savage and Morin, 2002; Schmitt, 1993; Warpinski and Teufel, 1991), lateral constraint stresses induced by Poisson's ratio expansion from the vertical gravitational loading (e.g., Amadei et al., 1988) and geothermal gradient (e.g., Sheorey, 1994; Sheorey et al., 2001), thermal anomalies (e.g., Haxby and Turcotte, 1976), and fluid flow (e.g., Chen, 2011;

Rice and Cleary, 1976), to name a few. Here we will assume for sake of a reference condition that the virgin stress tensor in the Earth is:

$$S = \begin{bmatrix} S_H & 0 & 0 \\ 0 & S_h & 0 \\ 0 & 0 & S_V \end{bmatrix} \tag{9}$$

with S_H, S_h, and S_V aligned with the x, y, and z axes, respectively. Later, this will be synonymous with the 'far-field' stresses of the rock mass into which the borehole is drilled.

The relative magnitudes of these three stresses with respect to one another strongly controls the motion of faults in the Earth and hence earthquakes and seismicity. These relative relationships are so critical to faulting theory applied by geophysicists and structural geologists that they serve as reference stress states and are introduced here to prepare for later discussion. Three different classes of fault motion result from three different combinations of these stresses as proposed by Anderson (1951) (see Kanamori and Brodsky, 2004). These three reference states (Fig. 2) are referred to as:

- Normal or extensional faulting regime: $S_V > S_H > S_h$
- Thrust faulting regime: $S_H > S_h > S_V$
- Strike slip faulting regime: $S_H > S_V > S_h$.

It should be remembered that this situation may not always hold in structurally complex zones (Yin and Ranalli, 1992).

In addition to the complementary planes along which shear faulting is expected, Fig. 2 also shows the planes that will open normal to the least compression during the formation of dykes (Ode, 1957; Paulsen and Wilson, 2010), joints (Engelder and Geiser, 1980), and hydraulic fractures (Hubbert and Willis, 1957). As will later be seen, the directions of such fractures are important pieces of information during field hydraulic fracturing tests.

It is often difficult to obtain truly *quantitative* measures of the complete, or even the partial, stress tensor of Eq. (9) including both magnitudes and directions. That said, a great deal can be accomplished as long as the type of faulting environment can be established.

2. Stress concentrations

Within a homogeneous Earth we do not expect large and rapid stress gradients. This situation changes drastically, however, once some kind of cavity such as a tunnel, a mine drift, or a borehole is introduced. This cavity is said to 'concentrate' the pre-existing stresses. Such stress concentrations can lead to failure of stressed objects and consequently are of great interest in fields such as mechanical engineering where many objects must have holes (e.g., Edwards, 1951; Pilkey et al., 2008) even at the nanometer scale (Ou et al., 2009). In this section we present the most common 2D and 3D cases for the stress concentrations around a circular borehole.

2.1. Concentration of far-field stresses: 2D Kirsch solution

We begin with the stress concentrations for the simplest case of a circular hole of radius a in a horizontal plate subjected to principal 'far-field' stress σ_{xx}. At a distance r from the hole axis and at azimuth θ measured with respect to the x-axis (Fig. 3) the hole redistributes the stresses in its vicinity to maintain equilibrium according to the classic 1898 solution of Kirsch (1898) with

$$\begin{aligned} \sigma_{\theta\theta} &= \frac{\sigma_{xx}}{2}\left(1+\frac{a^2}{r^2}\right) + \frac{\sigma_{xx}}{2}\left(1+\frac{3a^4}{r^4}\right)\cos(2\theta) \\ \sigma_{rr} &= \frac{\sigma_{xx}}{2}\left(1-\frac{a^2}{r^2}\right) + \frac{\sigma_{xx}}{2}\left(1+\frac{3a^4}{r^4}-\frac{4a^2}{r^2}\right)\cos(2\theta) \\ \tau_{\theta r} &= -\frac{\sigma_{xx}}{2}\left(1-\frac{3a^4}{r^4}+\frac{2a^2}{r^2}\right)\sin(2\theta) \end{aligned} \tag{10}$$

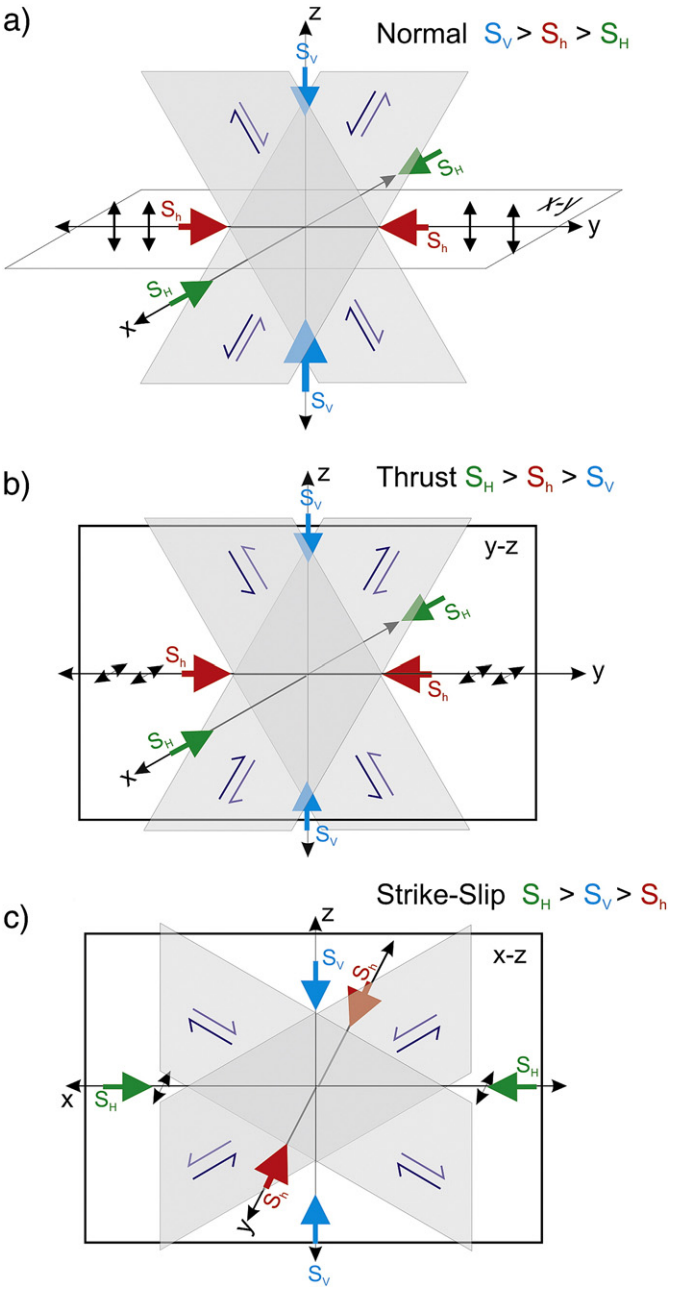

Fig. 2. Illustration of the three pure reference stress states with S_H, S_h, and S_V aligned with the x, y and z axes, respectively. In each panel, the two complementary planes of expected shear faulting are shown as transparent gray planes while the tensional opening occurs normal to the clear plane. a) Normal faulting with tensional opening normal to the x–y plane. b) Thrust faulting with tensional opening normal to the y–z plane. c) Strike-slip faulting with tensional opening normal to the x–z plane.

where σ_{rr}, and $\sigma_{\theta\theta}$ are the radial and azimuthal (hoop) normal stresses, respectively, $\tau_{r\theta}$ is the shear stress generated by the applied far-field stress and σ_{xx} is the radial distance r from the axis of the hole of radius a at the cylindrical co-ordinates (r,θ) (Fig. 3).

These stress concentrations can show some interesting patterns (Fig. 4). For example, if σ_{xx} is compressional, a pure hoop tension $\sigma_{\theta\theta} = -\sigma_{xx}$ is generated at points on the hole in the direction of σ_{xx} (i.e. $\theta = 0°$ and 180°) but perpendicular to this (i.e., at $\theta = 90°$ and 270°) the hoop stress is amplified to $\sigma_{\theta\theta} = 3\sigma_{xx}$. Kirsch's (1898) equations have long been applied in the geosciences to understand borehole stability (Bell and Gough, 1979), hydraulic fracture initiation

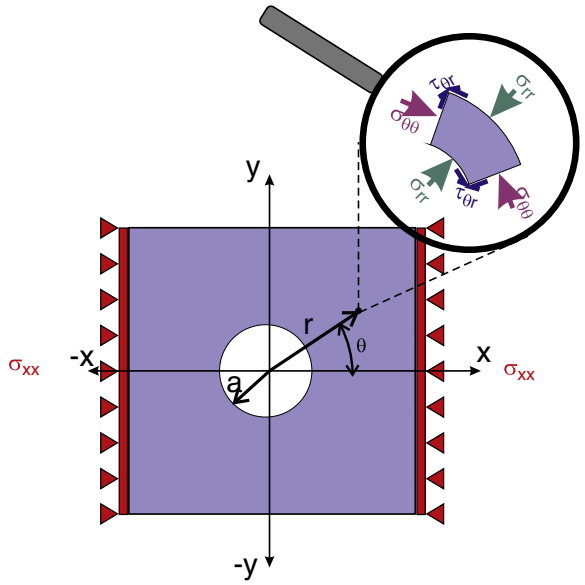

Fig. 3. Geometry of Kirsch's (1898) solution for the stress concentrations around a circular hole is a plate that is subject to a uniaxial stress σ_{xx}. Cylindrical element at location (r,θ) is magnified to show the cylindrical stresses acting on it.

(Hubbert and Willis, 1957), and mine stability (e.g., Li and Wang, 2008).

2.2. Concentration of far-field stresses: 3D

The Kirsch equations are derived under 2D plane conditions and as shown in Eq. (3) can only provide stress and displacement values within that plane. A real borehole is drilled in the 3D Earth where out of plane normal and shear stresses also exist. These stresses are illustrated for the general case of a long cylindrical cavity of radius a whose axis is arbitrarily oriented with respect to the principal stress state in the Earth. Fig. 5 shows two Cartesian co-ordinate frames with x–y–z having z aligned with the vertical and with x'–y'–z' aligned with the three principal stresses $[\sigma_{x'x'}, \sigma_{y'y'}, \sigma_{z'z'}]$, respectively. The x–y–z frame is conveniently chosen such that borehole axis projects onto the horizontal x-axis. Following Hiramatsu and Oka (1962), the y-axis passes through the origin perpendicular to the borehole axis that tilts at an angle ϕ relative to the x-axis. The third cylindrical r–θ–ζ co-ordinate frame is borehole centric with the ζ and borehole axes co-incident. As in Eq. (10), the angle θ is the azimuth with respect to the borehole axis.

In terms of the three far-field principal stress state $[\sigma_{x'x'}, \sigma_{y'y'}, \sigma_{z'z'}]$ and the direction cosines a_{ij} transforming the principal axes x'–y'–z' to the x–y–z frame the borehole centric stresses are (Edwards, 1951; Fairhurst, 1964; Hiramatsu and Oka, 1962)

$$
\begin{aligned}
\sigma_r &= \alpha_1\left(1-\frac{a^2}{r^2}\right)+\alpha_2\left(1-4\frac{a^2}{r^2}+3\frac{a^4}{r^4}\right)\cos 2\theta+\alpha_3\left(1-4\frac{a^2}{r^2}+3\frac{a^4}{r^4}\right)\sin 2\theta,\\
\sigma_\theta &= \alpha_1\left(1+\frac{a^2}{r^2}\right)+\alpha_2\left(-1-3\frac{a^4}{r^4}\right)\cos 2\theta+\alpha_3\left(-1-3\frac{a^4}{r^4}\right)\sin 2\theta,\\
\sigma_\zeta &= \beta_1-4\nu\left(\alpha_2\frac{a^2}{r^2}\cos 2\theta+\alpha_3\frac{a^2}{r^2}\sin 2\theta\right),\\
\tau_{\theta\zeta} &= \gamma_1\left(1+\frac{a^2}{r^2}\right)\cos\theta+\gamma_2\left(1+\frac{a^2}{r^2}\right)\sin\theta,\\
\tau_{\zeta r} &= \gamma_1\left(1-\frac{a^2}{r^2}\right)\sin\theta-\gamma_2\left(1-\frac{a^2}{r^2}\right)\cos\theta,\\
\tau_{r\theta} &= \alpha_2\left(-1-2\frac{a^2}{r^2}+3\frac{a^4}{r^4}\right)\sin 2\theta+\alpha_3\left(1+2\frac{a^2}{r^2}-3\frac{a^4}{r^4}\right)\cos 2\theta
\end{aligned}
\tag{11}
$$

where the coefficients

$$
\begin{aligned}
\alpha_1 &= \frac{1}{2}\Big\{\left(a_{x'x}^2\sin^2\phi+a_{x'y}^2+a_{x'z}^2\cos^2\phi-2a_{x'z}a_{x'x}\sin\phi\cos\phi\right)\sigma_{x'x'}\\
&\quad+\left(a_{y'x}^2\sin^2\phi+a_{y'y}^2+a_{y'z}^2\cos^2\phi-2a_{y'x}a_{y'z}\sin\phi\cos\phi\right)\sigma_{y'y'}\\
&\quad+\left(a_{z'x}^2\sin^2\phi+a_{z'y}^2+a_{z'z}^2\cos^2\phi-2a_{z'z}a_{z'x}\sin\phi\cos\phi\right)\sigma_{z'z'}\Big\},\\
\alpha_2 &= \frac{1}{2}\Big\{\left(-a_{x'x}^2\sin^2\phi+a_{x'y}^2-a_{x'z}^2\cos\phi+2a_{x'z}a_{x'x}\sin\phi\cos\phi\right)\sigma_{x'x'}\\
&\quad+\left(-a_{y'x}^2\sin^2\phi+a_{y'y}^2-a_{y'z}^2\cos^2\phi+2a_{y'z}a_{y'x}\sin\phi\cos\phi\right)\sigma_{y'y'}\\
&\quad+\left(-a_{z'x}^2\sin^2\phi+a_{z'y}^2-a_{z'z}^2\cos^2\phi+2a_{z'z}a_{z'x}\sin\phi\cos\phi\right)\sigma_{z'z'}\Big\},\\
\alpha_3 &= \left(a_{x'y}a_{x'z}\cos\phi-a_{x'x}a_{x'y}\sin\phi\right)\sigma_{x'x'}+\left(a_{y'y}a_{y'z}\cos\phi-a_{y'x}a_{y'y}\sin\phi\right)\sigma_{y'y'}\\
&\quad+\left(a_{z'y}a_{z'z}\cos\phi-a_{z'x}a_{z'y}\sin\phi\right)\sigma_{z'z'},\\
\beta_1 &= \left(a_{x'x}^2\cos^2\phi+a_{x'z}^2\sin^2\phi+2a_{x'z}a_{x'x}\sin\phi\cos\phi\right)\sigma_{x'x'}\\
&\quad+\left(a_{y'x}^2\cos^2\phi+a_{y'z}^2\sin^2\phi+2a_{y'z}a_{y'x}\sin\phi\cos\phi\right)\sigma_{y'y'}\\
&\quad+\left(a_{z'x}^2\cos^2\phi+a_{z'z}^2\sin^2\phi+2a_{z'z}a_{z'x}\sin\phi\cos\phi\right)\sigma_{z'z'},\\
\gamma_1 &= \left\{-a_{x'x}^2\sin\phi\cos\phi+a_{x'z}^2\cos\phi\sin\phi+a_{x'z}a_{x'x}\left(\cos^2\phi-\sin^2\phi\right)\right\}\sigma_{x'x'}\\
&\quad+\left\{-a_{y'x}^2\sin\phi\cos\phi+a_{y'z}^2\cos\phi\sin\phi+a_{y'z}a_{y'x}\left(\cos^2\phi-\sin^2\phi\right)\right\}\sigma_{y'y'}\\
&\quad+\left\{-a_{z'x}^2\sin\phi\cos\phi+a_{z'z}^2\cos\phi\sin\phi+a_{z'z}a_{z'x}\left(\cos^2\phi-\sin^2\phi\right)\right\}\sigma_{z'z'},\\
\gamma_2 &= \left(-a_{x'y}a_{x'z}\sin\phi-a_{x'x}a_{x'y}\cos\phi\right)\sigma_{x'x'}+\left(-a_{y'y}a_{y'z}\sin\phi-a_{y'x}a_{y'y}\cos\phi\right)\sigma_{y'y'}\\
&\quad+\left(-a_{z'y}a_{z'z}\sin\phi-a_{z'x}a_{z'y}\cos\phi\right)\sigma_{z'z'}
\end{aligned}
\tag{12}
$$

include the geometrical rotations through the direction cosines a_{ij} (Eq. (3)) and principal stress information. The reader should be aware that sign errors in the above have propagated through the literature, but Fjaer et al. (2008, Section 4.3) confirm that the Hiramatsu and Oka (1962) equations are correct.

The equations admit significant simplification at the borehole wall with $r=a$ if the borehole's ζ axis coincides with the co-ordinate frame's z axis (e.g., Cornet, 1993; Leeman and Hayes, 1966). In many cases it is assumed that the borehole is vertical (i.e. $\phi=\pi/2$) and Eqs. (11) and (12) reduce to

$$
\begin{aligned}
\sigma_{\theta\theta} &= \frac{\sigma_{xx}+\sigma_{yy}}{2}\left(1+\frac{a^2}{r^2}\right)-\frac{\sigma_{xx}-\sigma_{yy}}{2}\left(1+\frac{3a^4}{r^4}\right)\cos(2\theta)-\tau_{xy}\left(1+3\frac{a^4}{r^4}\right)\sin(2\theta)\\
\sigma_{\zeta\zeta} &= \sigma_{zz}-\nu\left\{2\left(\sigma_{xx}-\sigma_{yy}\right)\frac{a^2}{r^2}\cos(2\theta)+4\tau_{xy}\frac{a^2}{r^2}\sin(2\theta)\right\}\\
\sigma_{rr} &= \frac{\sigma_{xx}+\sigma_{yy}}{2}\left(1-\frac{a^2}{r^2}\right)+\frac{\sigma_{xx}-\sigma_{yy}}{2}\left(1+\frac{3a^4}{r^4}-\frac{4a^2}{r^2}\right)\cos(2\theta)\\
&\quad+\tau_{xy}\left(1+\frac{3a^4}{r^4}-\frac{4a^2}{r^2}\right)\sin(2\theta)\\
\sigma_{r\zeta} &= \left(\tau_{xz}\cos(\theta)+\tau_{yz}\sin(\theta)\right)\left(1-\frac{a^2}{r^2}\right)\\
\sigma_{r\theta} &= \tau_{xy}\left(1+2\frac{a^2}{r^2}-3\frac{a^4}{r^4}\right)\cos(2\theta)-\frac{\sigma_{xx}-\sigma_{yy}}{2}\left(1+2\frac{a^2}{r^2}-3\frac{a^4}{r^4}\right)\sin(2\theta)\\
\sigma_{\theta\zeta} &= \left(-\tau_{xz}\sin(\theta)+\tau_{yz}\cos(\theta)\right)\left(1+\frac{a^2}{r^2}\right).
\end{aligned}
\tag{13}
$$

It is interesting to note that these stress concentrations are mostly independent of the elastic properties of the rock save for Poisson's ratio ν.

2.3. Stresses arising from conditions in the borehole

One further consideration is that a real borehole in the Earth is usually filled with liquid be it water or dense drilling mud. As with all fluids the pressure in the mud column increases with depth. This fluid pressure P_w (here taken with a positive sign) is a boundary

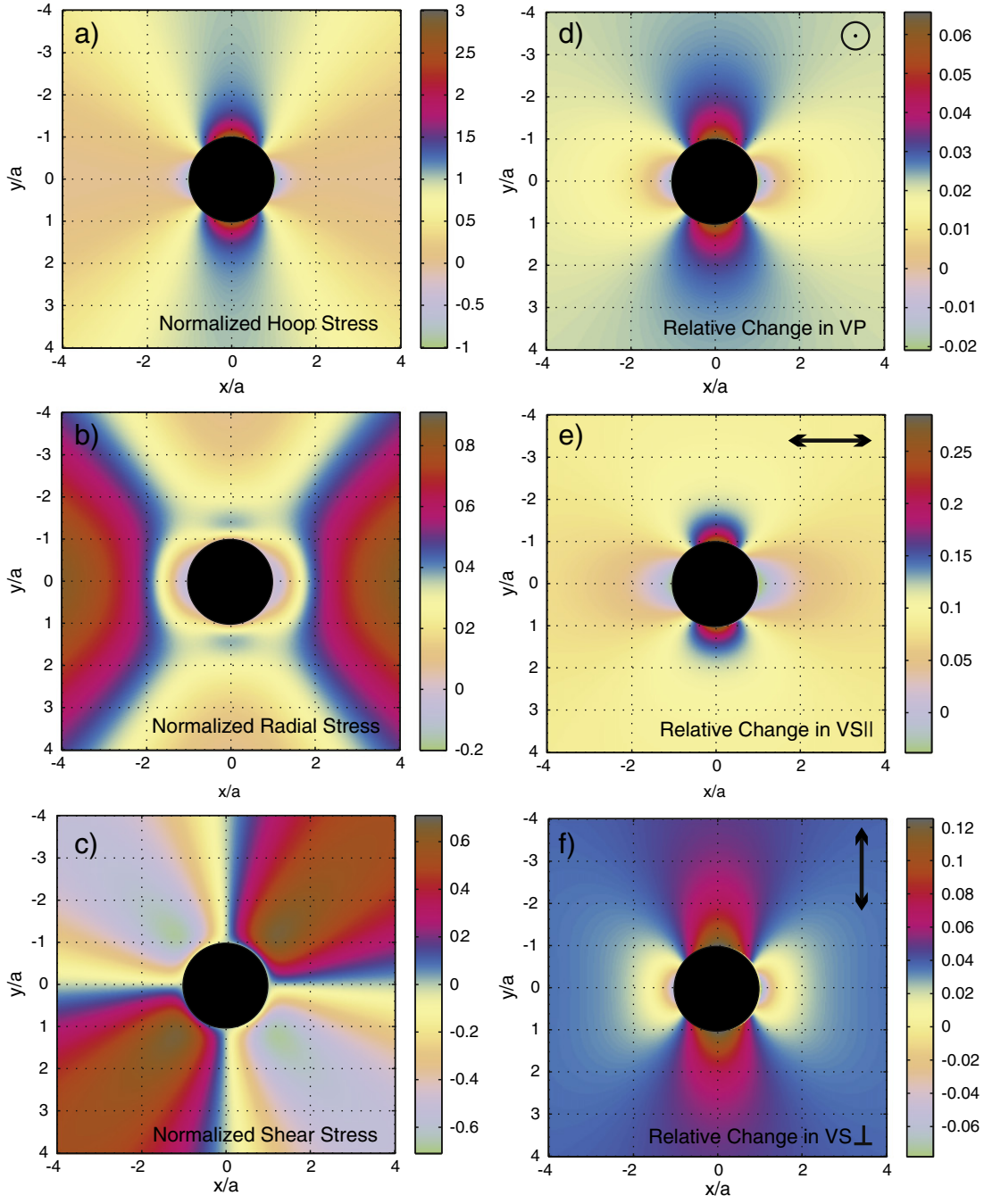

Fig. 4. Illustration of the distribution of the a) hoop stress $\sigma_{\theta\theta}$, the b) radial stress σ_{rr}, and the c) shear stress $\tau_{r\theta}$ concentrations in the vicinity of the hole in a plate of radius a subjected to a far field compressive stress σ_{xx} as shown in Fig. 3. The hole is empty and supports no stress. The stress magnitudes shown are normalized with respect to the magnitude of the far-field applied stress σ_{xx}. Pure tension is reckoned as negative in this figure. Effect of these stress concentrations on the speeds of the three waves propagating into the plane of the panels for d) the longitudinally polarized compressional wave, and the shear waves transversely polarized e) parallel or f) perpendicular to the direction of σ_{xx}. Calculations of the wave speeds follow Sinha and Kostek (1996) with Vp = 2320 m/s, Vs = 1500 m/s, ρ = 2062 kg/m3, $C111 = -21.21$ TPa, $C112 = -3.04$ TPa, and $C123 = 2.37$ TPa for $\sigma_{xx} = 2.0$ MPa.

condition on the wellbore wall that generates an axisymmetric stress field within the solid material $r \geq a$ that upon examination shows that a maximum tensile stress hoop stress $\sigma_{\theta\theta} = -P_w$ is generated immediately at the borehole wall with $r = a$. Eq. (14) derive from Lamé's solution for the stress concentrations in a long hollow cylinder (see Eqs. (44) and (45) of Timoshenko and Goodier, 1970)

$$\sigma_{rr}^{w} = P_w \frac{a^2}{r^2}$$
$$\sigma_{\theta\theta}^{w} = -P_w \frac{a^2}{r^2} \qquad (14)$$

and these are plotted in Fig. 6. Fluid pressure acting on the borehole always produces a tensile hoop stress and a compressive radial stress. Both of these are important when examining the failure of the borehole wall rock.

The above stress concentrations are primarily static in nature, but both temperature and pore fluid pressure diffusion from the borehole into the formation result in stress fields that vary with time. Analytic solutions exist but as these depend critically on the boundary conditions and material properties (that may also be temperature or pore pressure sensitive) and a wide variety of situations can be addressed. In both problems a diffusional equation must be solved; and the

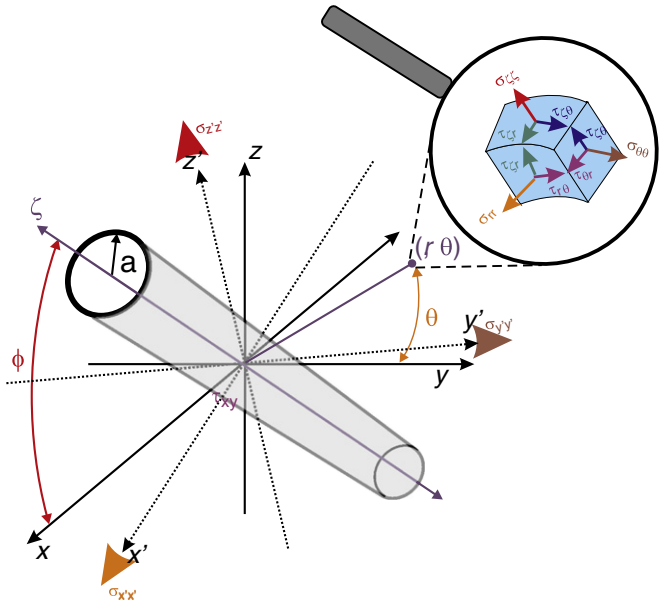

Fig. 5. Co-ordinate frames and borehole centric stresses for the problem of an arbitrarily oriented borehole.

solutions are analogous to one another to the point that both can share the same Fig. 7. As the potential situations that can be solved are vast, we rehearse here only two illustrative simple cases.

The first example is provided by Stephens and Voight (1982) who adapted Ritchie and Sakakura's (1956) thermo-elastic solutions for a hollow cylinder to study the stress concentrations at the borehole wall due to the application of a temperature T_w. This consists of a temperature gradient $\Delta T = T_w - T_\infty$ where T_∞ is both the initial uniform temperature of the system prior to perturbation and undisturbed temperature in the far-field of the borehole. Away from $r = a$ the solution depends on time as the temperature changes due to thermal diffusion, but immediately at the borehole wall the stresses are time independent as long as the temperature at the wellbore wall remains constant at T_w:

$$\sigma^T_{\theta\theta}(r=a) = \frac{\alpha E \Delta T}{1-\nu}$$
$$\sigma^T_{rr}(r=a) = 0 \qquad (15)$$

where α is the coefficient of thermal expansion. Increasing the temperature at $r = a$ effects a compressive hoop stress $\sigma_{\theta\theta}$ and vice versa. Although such thermal effects are usually ignored, examination of Eq. (15) shows that relatively large stresses are generated by modest changes in temperature (Fig. 7). For a typical quartz-rich granite

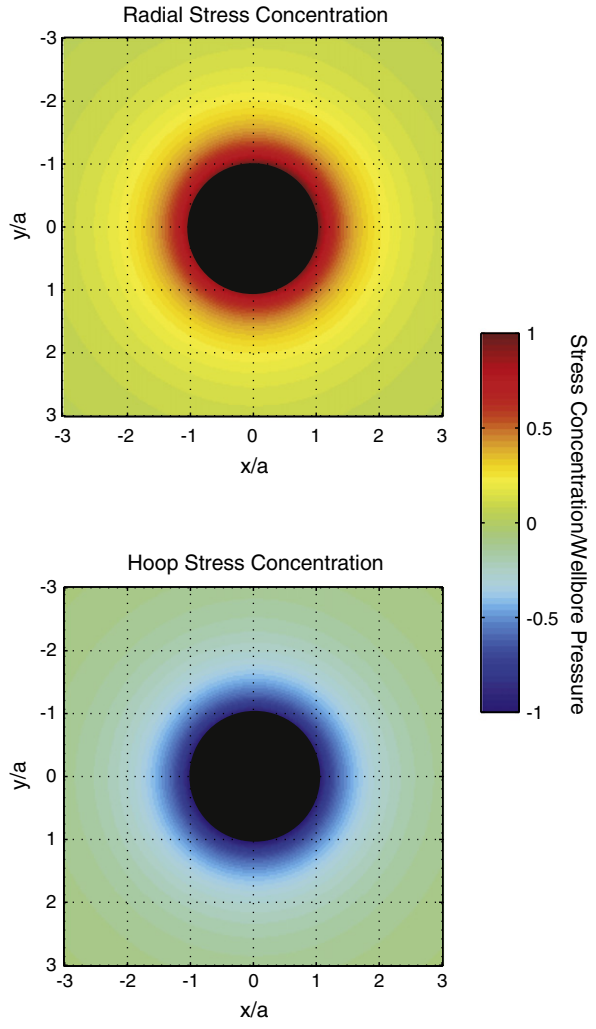

Fig. 6. Stress concentrations, normalized with respect to the wellbore fluid pressure, at the borehole wall resulting from the fluid pressures for the radial stress σ_{rr} (top panel) and the azimuthal hoop stress $\sigma_{\theta\theta}$ (bottom panel).

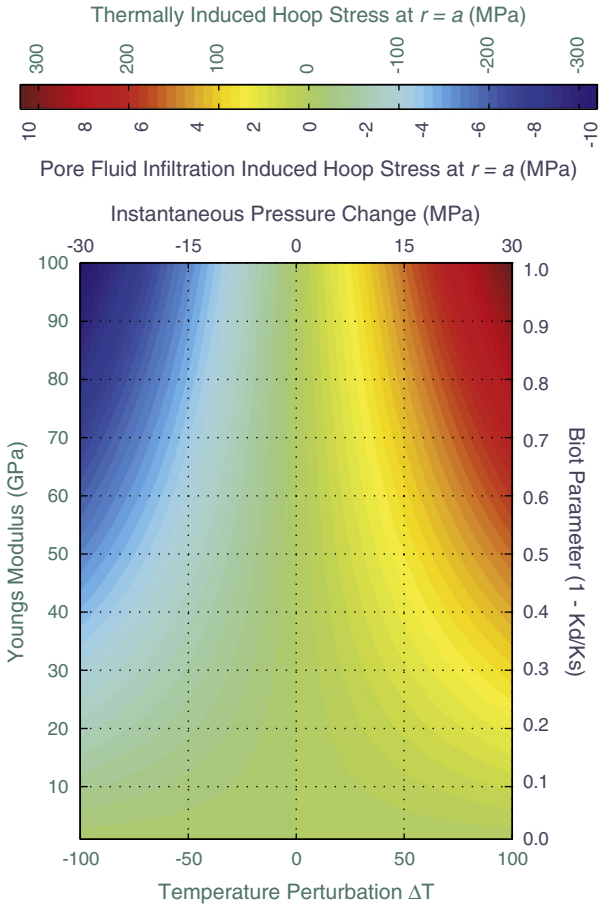

Fig. 7. Illustration of the magnitudes of the hoop stresses generated at the borehole wall $r = a$ for a poroelastic material of $\nu = 0.25$ and as a function of the material's Biot effective stress coefficient $1 - K_d/K_s$ (blue text — right axis), and an instantaneous pressure change ΔP according to Eq. (16) and of the magnitudes of the hoop stresses generated at the borehole wall $r = a$ for α material with $\alpha = 8 \times 10^{-6}$ °C and $\nu = 0.25$ as a function of the material's Young's modulus E (green text — left axis) and the temperature perturbation ΔT in degrees C according to Eq. (15). Tension is reckoned as negative.

with E~70 GPa a cooling of the wellbore wall by only 10 °C would generate a tensile stress $\sigma_{\theta\theta} = -22.4$ MPa, values that easily exceed the material's tensile strength. Indeed, Wu et al. (2007) employ temperature variations to control fracture propagation in hollow cylinders of acrylic.

Poro-elastic solutions for the stresses induced due to pore pressure diffusion are derived analogously (Haimson and Fairhurst, 1967; Rice and Cleary, 1976; Schmitt and Zoback, 1993). For example, the infiltration hoop stress generated at $r = a$ due to an instantaneous pressure change $\Delta P = P_w - P_o$ is given by

$$\sigma^I_{\theta\theta}(r = a) = -\Delta P(1-2\eta) \tag{16}$$

with

$$\eta = \frac{1}{2}\left(1 - {}^{K_d}\!/_{K_s}\right)\frac{1-2\nu}{1-\nu} \tag{17}$$

where K_d and K_s are the drained (or dry frame) and rock mineral bulk moduli, respectively. The term $1 - K_d/K_s$ is often called the Biot effective stress coefficient. The analogy between the thermal and fluid diffusion solutions is readily apparent in Fig. 7.

For purposes of simplicity later, we combine the stress concentrations resulting from wellbore fluid pressure, temperature differences, and pore pressure diffusion into a generic generated hoop stress $\Delta\sigma_{\theta\theta}$ at $r = a$ of

$$\Delta\sigma_{\theta\theta} = \sigma^w_{\theta\theta} + \sigma^T_{\theta\theta} + \sigma^J_{\theta\theta}. \tag{18}$$

2.4. Stress concentrations: additional considerations

The above equations assume an isotropic and linearly elastic rock mass and their examination reveals that, except for ν, the material properties are absent. However, real rock is usually much more complex (e.g., Giovanni, 1969) and solutions that consider the anisotropy of the rock mass (Amadei, 1983; Fairhurst, 1964; Wu et al., 1991) or time dependencies due to viscoelastic (Wawersik and Stone, 1989), elastoplastic (Papanastasiou and Durban, 1997) and poroelastic effects (Abousleiman and Chen, 2010; Detournay and Cheng, 1988; Rice and Cleary, 1976; Schmitt and Zoback, 1993), or nonlinear elasticity (Chin et al., 2000; Haimson and Tharp, 1974; Mahtab and Goodman, 1968; Meyer and Jacot, 2001; Mitaim and Detournay, 2004; Nawrocki, 2010; Santarelli et al., 1986) and chemical effects (Roshan and Rahman, 2011) have been developed. The problems of stresses near long cavities are still of current interest with recent applications of conformal mapping techniques applied to differing cross sections (Aadnoy and Angellolsen, 1995; Batista, 2010; Exadaktylos et al., 2003). However, nearly all stress analyses to date employ the simpler elastic solutions. The reader is referred to Fjaer et al. (2008) for a comprehensive overview of these problems that includes details of the equations used in a variety of cases.

3. Stress effects in rock

Rock is a complex material composed of solid minerals and fluid filled voids. Its mechanical properties depend critically on the composite structural architecture. Generally, the magnitude of the porosity is the first order control on such properties. However, the physical properties of rocks also depend on confining stress, the degree to which is controlled in some cases by Hertz–Mindlin grain contact responses (e.g., Makse et al., 1999) but more generally from crack-like porosity (see Sayers, 2010). Small aspect ratio (width to length) pore space strongly influences the stress and effective pressure response of rock, an attribute recognized in the first measurements on rock elasticity under pressure (Adams and Williamson, 1923; Zisman, 1933) and illustrated in Fig. 8.

Crack-like pore space, at any scale, is highly sensitive to the state of stress because even small stresses applied normal to the crack's plane readily push the crack's surfaces together. Indeed, idealized cracks close once the stress normal to their plane reaches a critical value p_c (the closure pressure) that for an elliptically shaped crack with ratio of minor to major axis χ is given by

$$p_c = \frac{\pi E \chi}{4(1-\nu^2)} \tag{19}$$

where E and ν are the Young's modulus and Poisson's ratio of the pore-free solid composing the material, respectively (Berg, 1965; Walsh, 1965). Note that p_c does not depend on crack length. Closing this crack makes the overall material stiffer; this nature makes both the rock nonlinearly elastic and allows for stress induced anisotropy.

One would expect a real rock to have a distribution of χs and hence closure pressures. It is this distribution of crack aspect ratios that leads to the progressive stiffening of the rock as the confining pressures increase (Meglis et al., 1996; Reuschlé et al., 2006) and the family of cracks with similar χs close. This progressive closure results in the nonlinear behavior for both elastic and transport properties (Han et al., 2011; Saner et al., 1996). The nonlinear pressure dependence of the wave speeds seen in Fig. 8 derives from such effects.

Numerous approaches have been used to describe this nonlinearity such as the Birch–Murnaghan equation of state with a pressure dependent variation in bulk modulus (Birch, 1961), higher order elastic constants (Payan et al., 2009; Sayers, 2007; Sinha and Kostek, 1996) or linearization of these (Gurevich et al., 2011), damage models (Lyakhovsky et al., 1997), wave speed to stress coupling coefficients (see Tang and Cheng, 2004), differentials related to crack closure (Ciz and Shapiro, 2009), or most commonly, by simply fitting to mathematical functions that parametrically mimic the rock behavior (Freund, 1992; Prikryl et al., 2005).

A second important implication of the stress sensitivity of cracks is that application of an anisotropic stress state induces elastic

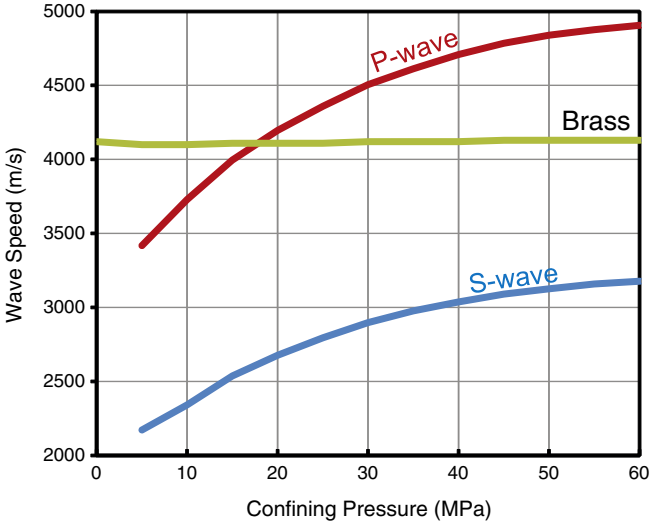

Fig. 8. Illustration of the effects of microcracks on the elastic properties of the Cadotte sandstone, Alberta, as manifested by the nonlinear relationship of the P- and the S-wave velocities with confining pressure. Nonporous brass shows little measureable change in P-wave speed over this pressure range.
Unpublished data from He (2006).

anisotropy in the rock. For example, a greater compression along one axis than another will result in greater crack closure and hence stiffness in that same direction as illustrated in Fig. 9. The top panel (Fig. 9a) shows the traces of a randomly oriented set of cracks in the initially unstressed and elastically isotropic rock. Uniaxial application of σ_{xx} (Fig. 9b) preferentially closes those cracks oriented such that the stress normal to their plane exceeds the crack closure pressure. The resulting material is now stiffer in the *x*-direction. However, those more horizontally aligned cracks stay open and the material remains compliant in the *y* direction. Consequently, the material becomes elastically anisotropic, and there are numerous examples in which this effect has been observed via ultrasonic measurements in cracked solids (e.g., Holt et al., 1993; Johnson and Rasolofosaon, 1996; Majmudar and Behringer, 2005; Nur and Simmons, 1969; Rathore et al., 1995; Sayers et al., 1990; Vilhelm et al., 2010; Wu et al., 1991; Zheng, 2000). In Fig. 9b crack closures produce a rotational symmetry around the *x*-axis that results in a transversely isotropic material (see Fuck and Tsvankin, 2009).

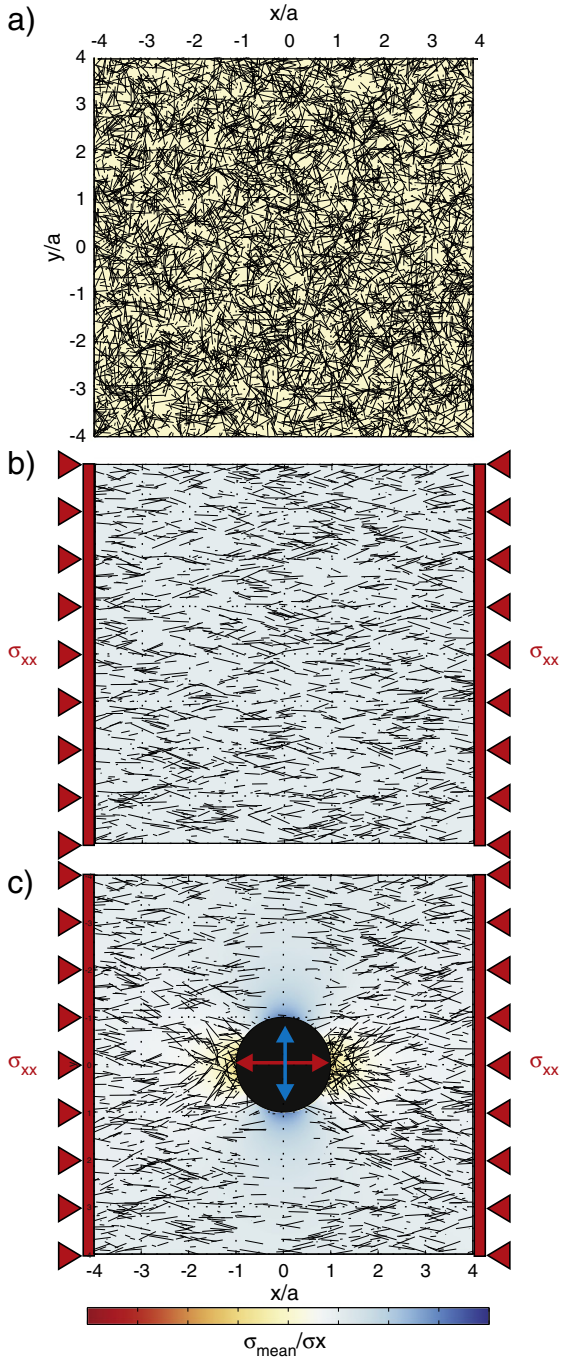

Fig. 9. Illustration of the effects of stress on crack closure within a rock, which under a) no confining stresses contains cracks (black lines) with a uniform distribution of orientations. b) Application of the uniaxial stress σ_{xx} preferentially closes those cracks subjected to normal stresses perpendicular to their plane exceeding the closure pressure. c) Drilling of the borehole through the rock results in stress concentrations that reopen cracks at the azimuth of the compression but close additional cracks perpendicular to this where the mean stresses are tensile or compressive, respectively. Color bar indicates the value of the normalized mean stress at each location with tension reckoned as negative.

Introducing a borehole and its consequent stress concentrations as described above (Fig. 4a–c) to this stressed rock mass results in a pattern of crack opening and closing azimuthally around the borehole axis (Fig. 9c). The mean stress $\sigma_{mean} = (\sigma_{xx} + \sigma_{yy})/2$ is a weak tension at the azimuths parallel to σ_{xx} with the result that the natural cracks remain open and the material is compliant. In contrast, σ_{mean} is compressive at those azimuths perpendicular to σ_{xx} such that more cracks are closed and the material is proportionally stiffer. In short, the rock elastic moduli vary azimuthally around the borehole axis due to the changes in the stress concentrations (Schmitt et al., 1989; Winkler, 1996).

The azimuthal variations in the rock compressibility, produced by the changing stress state near the wellbore, manifest azimuthal and radial dependencies of the speeds of the elastic waves propagating parallel to the borehole axis. An illustration of these variations, induced by the application of a uniaxial σ_{xx} and calculated with higher order elastic constants (Sinha et al., 1994) is found in Fig. 4d–f for the compressional and the primarily '*x*' and '*y*' polarized shear waves, respectively. These are included in Fig. 4 to allow for ready comparison to the same distribution of stress concentrations. To a large degree the wave speed variations mimic the pattern of the azimuthal hoop stress. The changes in the wave speeds are not insignificant and, as will be seen later, provide for methodologies for obtaining information on stress directions and perhaps even stress magnitudes.

Such variations have been measured directly. Gladwin and Stacey (1974), during thermal stressing of a tunnel, detected changes in the travel times of ultrasonic pulses of a few microseconds along paths of a few meters. Tang and Cheng (2004) provided evidence of two split shear wave arrivals with speeds differing by about 10% from monopole sonic log waveforms collected through a sandstone subjected to nonuniform horizontal stresses. Winkler and D'Angelo (2006) developed a high resolution technique to map the azimuthal evolution of the compressional speeds of waves propagating at the borehole wall and parallel to the borehole axis. Laboratory tests of the method in a borehole through a mass of uniaxially stressed sandstone showed that the wave speed increased by more than 17% at azimuths orthogonal to compression (Fig. 10a). More recently, Balland and Renaud (2009) developed an ultrasonic travel time tomography method that can map the compressional waves speeds both radially and azimuthally around the borehole. Their measurements (Fig. 10b) display the expected azimuthal velocity dependencies but also reveal a degree of damage that lowers the wave speed relative to the virgin formation. These last two examples clearly demonstrate the effects of stress concentrations on wave speeds around the wellbore, but as noted by Winkler and D'Angelo (2006) there are many technical challenges that must be overcome in order to implement such borehole measurements in a practical way.

4. Rock failure criteria

The discussions above have assumed that the rock, particularly in the vicinity of the borehole, behaves elastically; the rock has not been damaged. This case, while important, will be the exception especially for deeper boreholes that are subjected to increasingly higher states

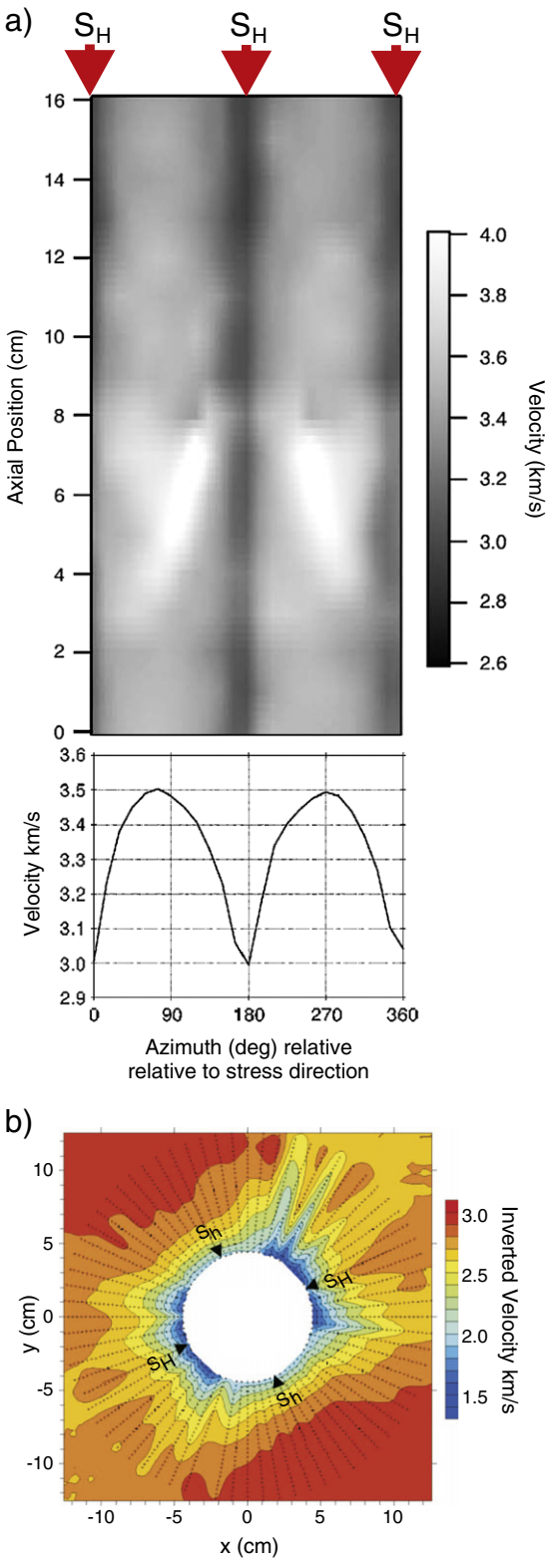

Fig. 10. Examples of stress induced velocity variations in the vicinity of a borehole. a) unwrapped image (top panel) of the apparent P-wave velocity parallel to the borehole axis as imaged along a laboratory test borehole subjected to a compression S_H of 10 MPa parallel to azimuths of $\theta = 0°$ and 180° and the corresponding average velocity (bottom panel) at each azimuth. Red arrows mark the azimuths at which the greatest compression is applied externally. b) Plan view looking down along the borehole axis velocities calculated using tomography and obtained along a number of differing radii. Panel a is adapted from Winkler and D'Angelo (2006). Panel b is from Balland and Renaud (2009). All figures used here are used courtesy of the Society of Exploration Geophysicists according to their reasonable use policy.

of stress. Consequently, more often than not the borehole wall rock will yield or completely fail. In this section a brief discussion of failure modes is provided in order to understand how they provide crucial diagnostics on in situ stress states.

By far, the most prevalent in the Earth mode of failure, which in nature is almost always in compression, is referred to as shear failure. Shear failure is most simply described using the Mohr–Coulomb frictional failure theory as summarized in many textbooks (Jaeger et al., 2007; Zoback, 2007) where details are available. The geometry of the failure is given in Fig. 11a and these criteria state that shear failure occurs when

$$\tau = \sigma\mu + C \tag{20}$$

where τ and σ are the shear and normal stresses, respectively, on the incipient failure plane, μ is the coefficient of internal friction and C is the 'cohesion' in units of stress. The internal friction μ controls the angle γ with respect to σ_{max} of the plane along which shear failure will occur

$$\gamma = \frac{\pi}{4} + \frac{\arctan[\mu]}{2}. \tag{21}$$

The reader should not be left with the impression that the Mohr–Coulomb model is the only one describing shear failure and numerous additional criteria have been developed under various assumptions. While in later sections the use of various criteria is mentioned in

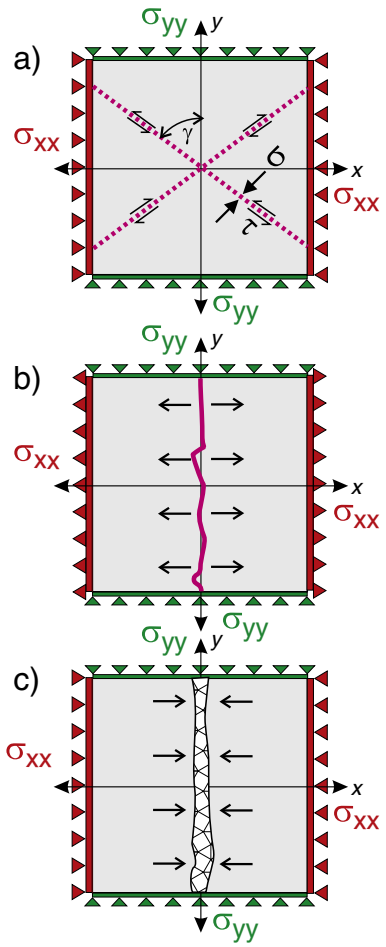

Fig. 11. Illustration of the modes of rock failure. a) Shear failure under compressive stress state $\sigma_{xx} > \sigma_{yy}$, b) tensile failure produced by pure tension σ_{xx}, c) compaction band collapsing parallel to $\sigma_{xx} > \sigma_{yy}$.

the context of the stress measurement techniques there is insufficient space here to devote to describing the rapidly growing literature on this topic (Al-Ajmi and Zimmerman, 2006; Colmenares and Zoback, 2002; Haimson and Chang, 2002; Zhang et al., 2012).

Tensile stresses are not generally expected to exist under normal conditions in the Earth and as such this failure mode (Fig. 11b) is not as well studied in rocks. However, they can exist as shown above due to the stress concentrations around the borehole. In this case, a very simple criterion first attributed to Rankine can be applied that states that tensile (pulling apart) failure will occur if the most tensile (least compressive) principal stress exceeds the 'tensile strength' T_o of the material. In such a case the tensile fracture will open in the direction of this tensile stress.

While we mostly consider shear and tensile failure it is worth mentioning more recent developments with regards to compaction bands (Fig. 11c). These are highly localized zones characterized by overall densification and micro-crack damage to the mineral grains observed in porous sandstones. They do not display any shear offset suggesting that they 'close' perpendicular to the greatest compression (Mollema and Antonellini, 1996) with loss of volume and hence can be called anti-mode I failure. This deformation mode has garnered a great deal of attention due to its application to consolidation of reservoirs, production of sand during fluid extraction, and the creation of certain classes of borehole breakouts (Katsman and Haimson, 2011; Schultz, 2009; Stanchits et al., 2009; Tembe et al., 2008).

5. Stress measurement techniques

The above sections on stress concentrations, on the nonlinear elastic responses of rocks, and failure modes in rock all provide essential background information in order to understand how to interpret observations from cores and boreholes. As noted earlier it is often not so much the stress that is measured directly, but rather its manifestations in a perturbed Earth. The stress concentrations as shown by Kirsch's (1898) solutions above illustrate this well. The only way for us to directly sample into the Earth is by creating a cavity. This cavity must concentrate the stresses as shown in Fig. 4 and the resulting patterns of the disruption, whether by elastically changing the physical properties or by actually damaging the borehole wall rock, can be measured. These stress concentrations amplify the virgin in situ stresses and produce substantive anisotropy of the elastic properties or can lead to different kinds of failure of the borehole. The latter is of particular economic concern as unstable borehole conditions can be costly to drilling operations.

5.1. Crossed dipole sonic logging

In analogy to surface waves in seismology and light transmission through optical fibers, a family of various borehole wave modes exists. These include tube, pseudo-Rayleigh, screw, and quasi-flexural waves. Much like surface Rayleigh and Love waves, these borehole modes are dispersive, and their phase wave speeds are controlled by a number of factors that include the variations in the physical properties of the wellbore fluid and of the rock in the vicinity of the borehole and the borehole dimensions. Consequently, much like Rayleigh wave inversion of surface data, detailed analysis of the borehole modes allows information on changes in physical properties near the borehole. The fact that these variations depend on the distribution of stresses (Fig. 4e–f) suggests further that the results can be interpreted to provide information on the horizontal stress directions and perhaps magnitudes (Frignet et al., 1999; Murray et al., 2004; Plona et al., 1998, 2002).

The 'flexural' mode of oscillation is most germane to stress indication. The particle motions associated with this mode are reminiscent of the transverse oscillations one might observe in the various modes of transverse vibrations seen in a string under tension although the flexural waves can have any frequency (Fig. 12). From a vertical borehole quasi-flexural waves are distinguished by horizontal particle motions and phase velocities *VF* that correlate with the (primarily) phase speed velocities of the radially polarized shear waves, for this discussion denoted as $VS(r,\theta)$, that are also propagating parallel to the borehole axis. This effect serves as the basis for the 'crossed-dipole sonic' method that is widely used to estimate the direction of the principal horizontal stresses and the degree of anisotropy. Technical details of how the measurements are made are beyond the space available here and the reader is directed towards Tang and Cheng (2004). Briefly, however, a 'dipole', or 'bender' acoustic transmitter produces a radial but uni-directional 'push–pull' displacement in the wellbore fluid that preferentially excites the flexural mode (Zemanek et al., 1984).

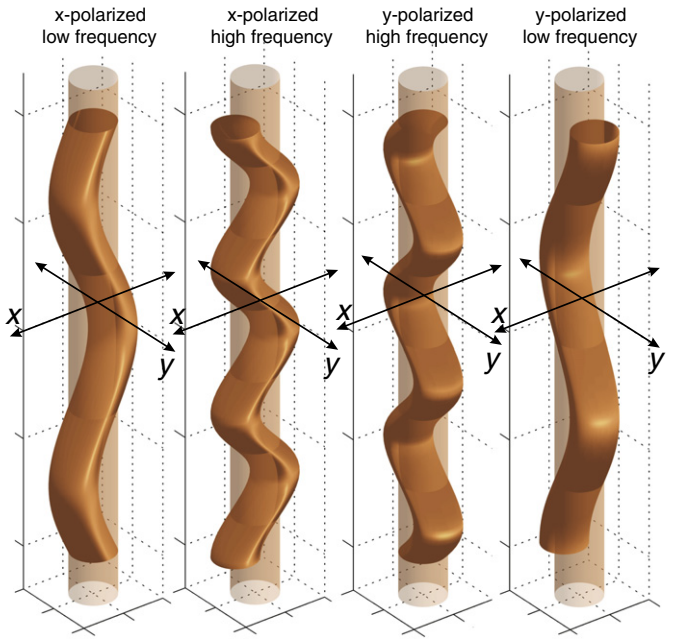

Fig. 12. Exaggerated illustration of the high (short wavelength) and low (long wavelength) frequency particle motions associated with two orthogonally polarized flexural modes excited from a vertical borehole. These would be the polarizations enforced by intrinsic or stress induced anisotropy (see Fig. 13b,c).

In an isotropic formation the borehole will flex in the direction of the provided push–pull. In contrast, in an anisotropic formation both the fast and the slow flexural waves are generated with particle motions dictated, as just described, by the directions of the anisotropy. Further, their respective amplitudes are controlled by the azimuth at which the push–pull is directed. For example, if the push–pull displacements are aligned with the material's rotational axis of symmetry then only the slow flexural wave (in blue in Fig. 13b) results. If the push–pull is at 45° to the symmetry axis, then both the fast and slow flexural waves are created. Geometry stipulates that this information cannot be found with only a single set of oriented dipole sources and receivers; and for this reason a second set of transducers that gives a perpendicular push–pull is added. At each depth two in-line and two crossed waveforms are acquired and these are processed using schemes developed for the analysis of multi-component seismic waves (Esmersoy et al., 1994). This 'crossed-dipole' analysis finds that the 'fast' and 'slow' azimuths, and hence those for S_H and S_h, respectively, would be encountered in the far-field from the borehole in Fig. 9c.

Again, as with surface waves on the Earth, the longer the wavelength of the flexural wave the deeper into the formation the wave senses and at sufficiently long wavelengths *VF* approaches *VS*. At lower frequencies $VF<VS$. $VF(r)$ depends on $VS(r)$; and hence measuring $VF(r,\theta)$ provides proxy information on $VS(r,\theta)$.

Fig. 13 provides three examples of differing velocity structures in the vicinity of the borehole and how these would affect the *VF* dispersion.

In the first (Fig. 13a) the borehole is drilled into an elastically isotropic formation; *VS* is constant for all propagation directions and polarizations. Correspondingly, there is no restriction on the azimuth θ

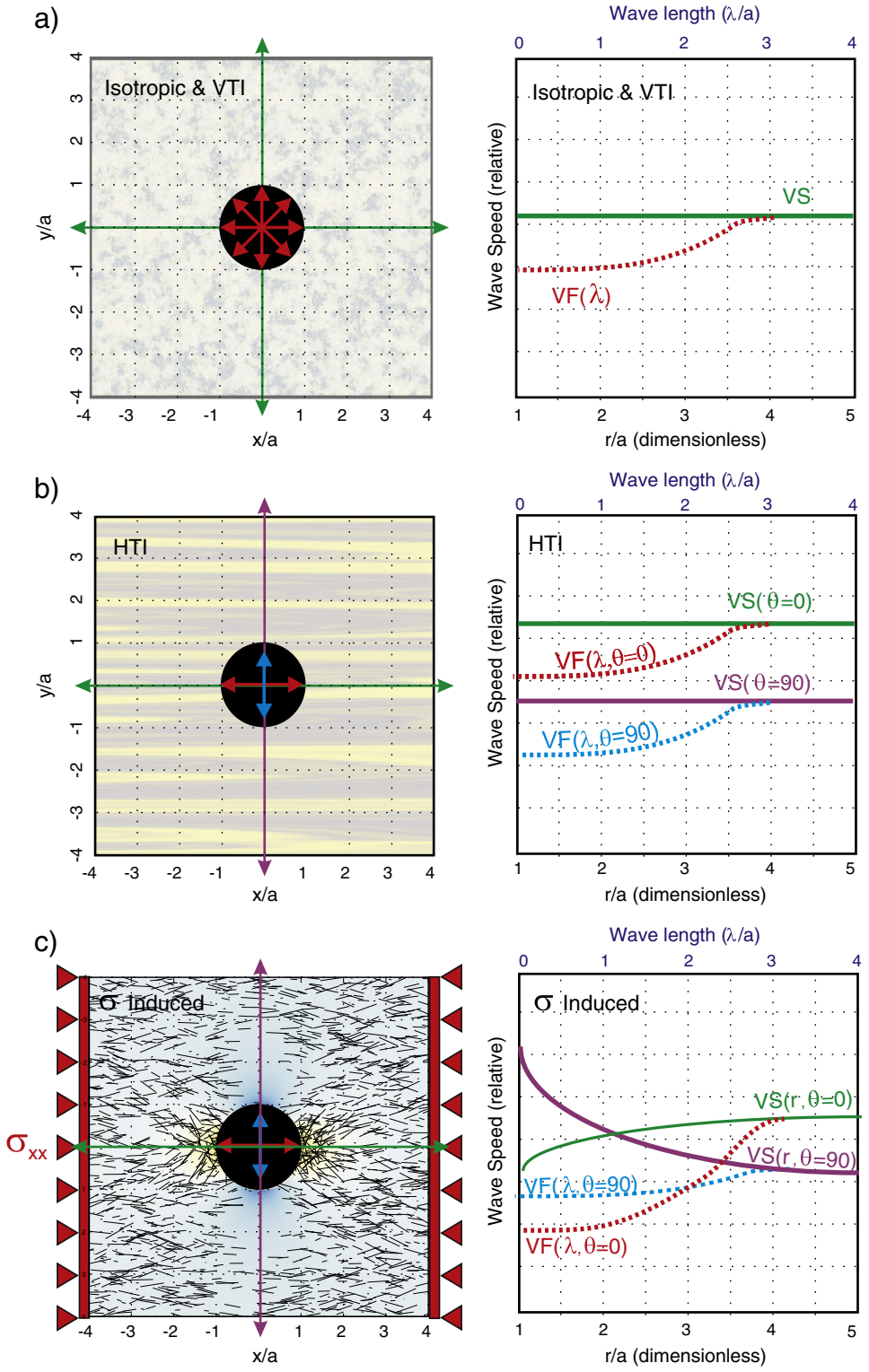

Fig. 13. Illustration of various examples of the effects of the variations in the radially polarized shear wave velocity *VS* versus normalized radial distance *r*/*a* from the borehole axis on the dispersive flexural wave velocity *VF* versus wavelength. Red and blue arrows indicate allowed flexural wave displacements. Borehole is vertical and the flexural waves propagate parallel to its axis. a) Isotropic or VTI symmetry: there is no enforced flexural wave polarization direction and flexural wave velocity (red dashed line) approaches *VS* (constant green line) with increasing wavelength (decreasing frequency). b) Intrinsically anisotropic HTI formation with $VS(\theta=0^\circ) > VS(\theta=90^\circ)$ the flexural wave polarizations are only allowed in the *x* and *y* directions and the two associated flexural wave dispersion curves (red and blue dashed lines, respectively) do not cross and approach $VS(\theta=0^\circ)$ (constant green line) and $VS(\theta=90^\circ)$ (constant purple line), respectively. c) Stress induced radial and azimuthal velocity variations: $VS(r,\theta=0^\circ)$ and $VS(r,\theta=90^\circ)$ cross also resulting in the crossing of the corresponding *VF* dispersion curves.

at which the flexural mode can be polarized; and the generated flexural wave will be polarized in the direction of the 'push–pull' motions of the tool. The observed flexural wave dispersion $VF(r)$ depends only on the frequency, or as shown in Fig. 13 with the wavelength λ.

The next level of complexity considers the case of a vertical borehole through an intrinsically horizontal transversely isotropic (HTI) formation (Fig. 13b). Such a case could exist if an otherwise elastically isotropic formation contains an oriented set of vertical fractures, or if the rotational symmetry axis of a layered sediment is tilted horizontally. Ellefsen et al. (1991) showed in this instance i) that two flexural modes exist, ii) that both modes are orthogonally polarized with horizontal particle motions parallel to the polarizations of the fast and the slow shear body waves propagating parallel to the borehole axis, and iii) that the speeds of these polarizations are also fast and slow, respectively, relative to one another. Hence, the two flexural wave polarizations and wave speeds contain information on the degree and orientation of the material's intrinsic anisotropy.

Consequently, if the anisotropy is stress induced, as in the case illustrated in Fig. 9b, then the long wavelength components of the flexural waves can provide information on the direction of the principal stresses (Fig. 13c). Further examination of Fig. 9c and of Fig. 4e–f shows that the stress induced wave anisotropy near the borehole is considerably more complex than for intrinsic formation or stress induced anisotropy alone (Fig. 13a,b). At the σ_{xx} azimuth, the radially polarized shear wave velocity is lower than normal (Fig. 4e) whereas perpendicular to this the wave speed is considerably higher (Fig. 4f). The relation reverses in the 'far-field'. As noted, the various wavelength components will also sense these changes. At higher frequencies (smaller wavelengths) the flexural waves are most sensitive to the properties near the wellbore, while the lower frequency waves sense deeper into the formation (Pistre et al., 2005; Sinha et al., 1994). This results in a frequency dispersion of the flexural wave speeds with a further characteristic that the dispersion curves (dashed lines, Fig. 13c) for the two perpendicular polarizations cross (Winkler et al., 1998). In contrast, there is no radial dependence on the shear wave speeds in the more general intrinsically anisotropic formation and consequently the dispersion curves of the x and y polarizations are offset but do not cross (dashed lines, Fig. 13b). Examination of such dispersion curves allows stress induced anisotropy to be distinguished from intrinsic anisotropy (Boness and Zoback, 2006). Further, there have been attempts to employ information from the dispersion curves to provide quantitative measures of S_H (Lei et al., 2012; Sinha et al., 2008) although calibrations of these type of measurements suggest that the material properties and their stress dependencies must be well known (Ashraf Mohammed and Abousleiman, 2008) and it is not understood yet whether this technique is able to provide reliable stress magnitudes.

5.2. Hydraulic fracturing and leak off testing

The hydraulic fracture technique is usually accepted as providing the most robust quantitative values for the in situ stress magnitude, particularly S_h. In this method, an artificial hydraulic fracture is created by rapidly pressurizing a sealed section of a wellbore until the in situ stresses and the rock strength are overcome and a fracture propagates away from the borehole (Fig. 14). The fracture will continue to extend into the geological formation; the fracture essentially increases the effective surface area of the borehole and allows much larger volumes of fluid to be extracted. Because the fluid pressures involved must overcome the stresses and the material strength in order to initiate, propagate, and remain 'open', the pressurization histories conversely contain a great deal of information on the in situ state of stress.

A detailed description of a hydraulic fracturing stress measurement procedure is given by Haimson and Cornet (2003) and Zoback (2007) and only a brief outline is necessary here. Indeed, a simplified

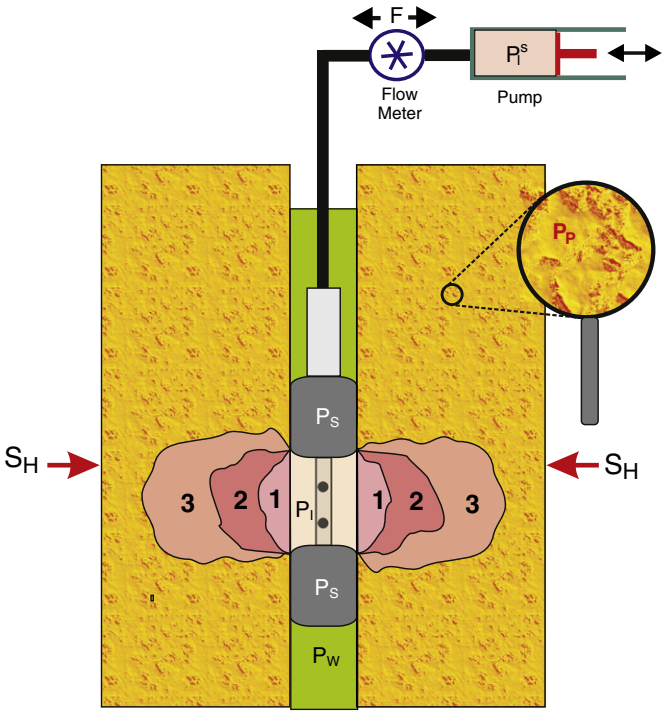

Fig. 14. Outline of the principal components of a hydraulic fracturing stress measurement. An interval along the borehole is isolated by two inflatable packers to pressure P_S. The pressure in the interval P_I is then increased from ambient well bore pressure P_W by pumping fluid in. The interval pump pressure at the surface is P_I^S and the fluid flow rate F into or out of the interval is measured by the flow meter. The induced fracture extends successively with each of three P_I pressurization cycles in the direction of S_H and opens against S_h. The pore pressure in the formation is P_P.

discussion of the pressurization record obtained is provided that illustrates only the essential elements while ignoring its finer details, the interpretation of which is beyond the scope of this article (Gjonnes et al., 1998; Hayashi and Haimson, 1991; Ito et al., 1999; Nelson et al., 2007). In open-hole (i.e. uncased) boreholes, a typical hydraulic fracturing test (Fig. 14) begins with sealing of an interval along the borehole with two packers. Here, for purposes of illustration the ideal case of hydraulic fracturing from a borehole drilled parallel to the vertical stress into a linearly elastic, nonporous material with tensile strength T_o is considered. A simplified and hypothetical pressurization record illustrates the process (Fig. 15) with three pressurization cycles (Rutqvist et al., 2000).

In the first cycle, the interval is first rapidly pressurized from the ambient P_o until a rapid drop in the interval pressure P_I occurs even if pumping to the interval continues; the maximum value of P_I is called the break-down pressure P_B. The drastic reduction in pressure results from the abrupt increase in the interval volume due to the incipient opening of the fracture.

At this point the pumping ceases and the interval is 'shut-in'; P_I then relaxes to an equilibrium pressure P_{SI}. Once it is away from the borehole stress concentrations the fracture will open in the direction of the least compressive stress (Hubbert and Willis, 1957; Murdoch, 1995; Warren and Smith, 1985). This may be complicated by horizontal fractures that intersect the borehole (e.g., Evans et al., 1988) or by heterogeneities in the rock mass (Warpinski and Teufel, 1991). Hence, once the fracture exists it can remain jacked open as long as equilibrium exists and the interval pressure P_{SI} is at least equal to the minimum compression which is S_h for strike-slip and normal faulting and S_V for thrust faulting regimes. Indeed, an accurate determination of P_{SI} is usually taken as the most robust stress magnitude measurement available. However, even this assumption may not always be valid (Nelson et al., 2007) and the fact that many different

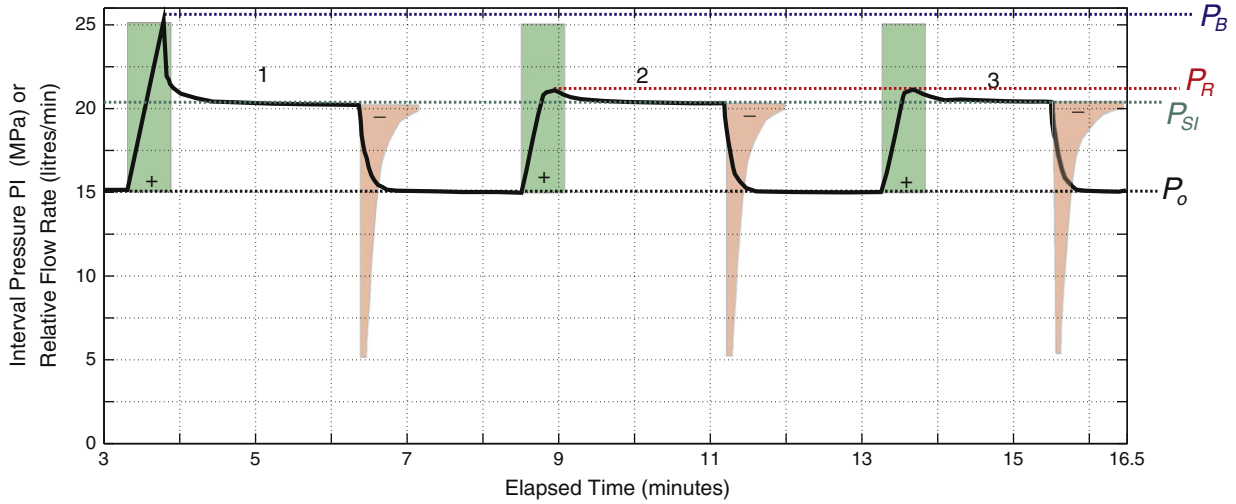

Fig. 15. Illustration of a typical hydraulic fracturing (micro-frac) stress measurement. Heavy black line represents the pressure recorded within the interval. Green and red shaded areas represent flow rates into or out of the interval, respectively.

techniques have been developed to find P_{SI} may hint at some ambiguities in its determination (Guo et al., 1993; Ito et al., 1999).

After an appropriate equilibration, the interval pressure is released and decays back to the ambient borehole pressure prior to the experiment. The excess fluid in the interval will flow back to the surface reservoirs.

The cycle is repeated a number of times. On the second cycle the pressure increases until the already created fracture reopens. Again a rapid drop in the pressure accompanies the increased volume, but the interval pressure P_R at which this occurs is smaller than P_B because the rock's tensile strength no longer needs to be overcome, this issue is discussed in more detail below.

As already noted P_{SI} gives a reliable quantitative measure of the minimum compression in the Earth. In addition, however, P_B and to some extent P_R contain information on the stress concentrations immediately at the borehole wall ($r=a$). For the simple case above, the incipient fracture initiation occurs when the P_I induced $\sigma_{\theta\theta}$ tension (Eq. (14)) overcomes both T_o and the concentrations of the S_H and S_h; this will happen at the S_H azimuths ($\theta=0°$ and 180°). This allows the stress directions to be found from oriented images of the borehole although care here must, too, be taken (Evans et al., 1988; Warren and Smith, 1985). Consequently, at breakdown ($P_I=P_B$) and where $P_{SI}=S_h$ the maximum horizontal compression is

$$S_H = 3S_h + T_o - \Delta\sigma_{\theta\theta} \tag{22}$$

where $\Delta\sigma_{\theta\theta}$ was described earlier (Eq. (18)). Eq. (22) is the simplest 'break down' equation that can be written but is deficient in that it excludes potentially important factors such as the ambient pore pressure, the fluid pressure in the incipient fracture, or interval pressurization rate effects (Schmitt and Zoback, 1992). The reader may find derivations of the appropriate corrections in numerous contributions (e.g., Schmitt and Zoback, 1993). Kehle (1964) carried out a more sophisticated analysis that incorporated the influence of the sealing packers on the stress concentrations and found that it remains valid, although his analysis did not include the radial pressure of the packers themselves, a deficiency later resolved by Warren (1981) who warned about issues in interpreting P_B if the packer pressure significantly exceeds P_w. The values of S_H that were determined, however, are taken to be uncertain because often even if one could presume to know exactly the physics operating during creation of the fracture leading to breakdown (e.g., Golshani and Tran-Cong, 2009), obtaining the appropriate physical properties needed is difficult and often only estimates can be made.

As well, it is often not known whether the fracture initiation is influenced by the packers themselves; owing to the design of the system they must remain at a pressure above that in the interval (Warren, 1981; Warren and Smith, 1985). One final caution comes when measurements are made in thrust fault regimes where S_V is the minimum compression, Evans et al. (1988), for example, observed that both horizontal and vertical fractures were produced during hydraulic fracturing tests in granite and noted the ambiguities that arise in attempting to interpret the pressurization curves in thrust regimes.

The survey of the history of the 'tensile strength' T_o employed highlights some of the difficulties encountered in trying to obtain an accurate quantitative measure of S_H. Hubbert and Willis (1957) were the first to provide a formula akin to Eq. (22) that related the state of stress to the fluid pressure in order to estimate both S_H and S_h but reasoning that rock formations are already densely populated with joints of negligible cohesion they neglected to include any formation strength in their analysis (as noted by Scheidegger, 1960). Kehle (1964) incorporated a tensile fracture criteria for initiation that, given the limited knowledge of tensile rock strengths at the time, assumed a constant value of 20 MPa. Later field campaigns used laboratory T_o derived from Brazilian tests of laboratory hydraulic fracture simulations on core samples (Raleigh et al., 1972; Yamashita et al., 2010).

Beginning with Bredehoeft et al. (1976) many workers have suggested that the difference $P_B - P_R \approx T_o$ predicated on the assumptions that on the second and later pressurizations the already existing fracture retains no tensile strength, that the stress concentrations and pore fluid pressures remain the same both before and after creation of the fracture, and that the pressurizing fluid does not re-enter the crack until its P_R is attained (e.g., Healy and Zoback, 1988; Hickman and Zoback, 1983; Stock et al., 1985). In this case Eq. (22) reduces to

$$S_H = 3S_h - P_R. \tag{23}$$

A considerable simplification is S_h has been correctly determined from P_{SI}. The validity of these assumptions has been questioned by numerous authors. Ratigan (1992) noted that once the crack is produced the stress state is altered and that the P_R responds to fracture geometry, fluid viscosity, and injection rates in addition to the stress concentrations. He showed that, generally, the use of P_R in Eq. (23) depends on the distance that the initial crack had grown into the formation, a difficult parameter to obtain. Ito and Hayashi (1993) also carried out a fracture mechanics analysis of a pre-existing horizontal

crack from a vertical borehole. Their calculations, supported also by experiments, indicated that P_R was closer to the magnitude of the applied S_V. Later, Ito et al. (1999) showed by simply superposing the added stress induced by pressurized fluid in the already existing crack that Eq. (23) would be modified to

$$S_H = 3S_h - 2P_R. \quad (24)$$

inferring Eq. (23) overestimates S_H. Their analysis went further, however, and included the influence of the overall compliance of the system including the hydraulic fracturing hardware which brought to light a more serious problem that the pressurization record alone may not correctly give the correct P_R. In parallel, Rutqvist et al. (2000) carried out numerical simulations of reopening that demonstrated that the apparent P_R is close to P_{SI} and this too will depend on the hardware compliance. In short, although Eq. (23) is widely employed, the above analyses show this may seriously overestimate S_H. Raaen et al. (2006) provide a recent overview of this problem and make suggestions for overcoming this using flow back monitoring in extended leak-off tests.

In their important paper, Hubbert and Willis (1957) noted that the preferred plane of a hydraulic fracture is perpendicular to the direction of the least compressive stress as discussed earlier in Section 1.2. The minimum injection pressures must be consequently equal to either S_h for the former two cases and S_V for the latter. Evidence for this came from field observations of dyke orientations and from simple illustrative laboratory tests in blocks of gelatin subjected to various loads. That is again following Anderson's (1951) studies of dyke propagation, vertical fractures are expected in normal and strike-slip regimes while horizontal fractures would propagate in normal faulting regimes (Fig. 2). Consequently, the normal to the plane of an induced hydraulic fracture clearly indicates the direction of the minimum compression while the plane itself must contain the greatest and intermediate stress directions. This was later confirmed by Haimson and Fairhurst (1969) who were able to propagate both vertical and horizontal fractures in laboratory tests (see also Daneshy, 1971). In combination with the stress concentrations at the borehole wall this means that the induced fracture will appear at the azimuths at which the spring-line of S_H intersect the borehole wall; hence measuring the direction of these new fractures reveals the S_H direction. A variety of methods have been developed to find these fracture directions. These include the use of oriented soft polymer 'impression' packers (Fig. 16a) that are set over the fractured zone (e.g., Haimson et al., 2003; Teufel et al., 1984) or various geophysical logs that image the borehole wall (Fig. 16b) such as ultrasonic borehole televiewers (Bredehoeft et al., 1976; Schmitt et al., 2012). However, some care must be exercised in the interpretation of the borehole wall fractures as they may not always indicate the true orientations of the propagating fracture away from the zone of influence of the stress concentrations. For example, even though the induced fracture is seen running parallel to the borehole axis the growing fracture plane will rotate to accommodate the virgin stress state away from the borehole (e.g., Daneshy, 1971).

To conclude this section, it is worth mentioning that there are a number of variations on this theme that may be advantageous under certain conditions. These include sleeve fracturing (Stephannson, 1983), development of 4-packer systems for high stress conditions (Ask et al., 2009), use of small pilot holes at the end of the main borehole (Ito et al., 2006), rapid deployment of packers using wire-lines (Klee et al., 2011; Schmitt et al., 2011), and use of expendable aluminum packers in high temperature geothermal environments (Klee and Rummel, 1993). Opening of pre-existing fractures, too, has been developed into a methodology to obtain the complete state of stress from a borehole. In this method, called the hydraulic tests on pre-existing fractures (HTPF) method, the results of a number of re-opening tests on variously oriented fractures is inverted to obtain and estimate the full

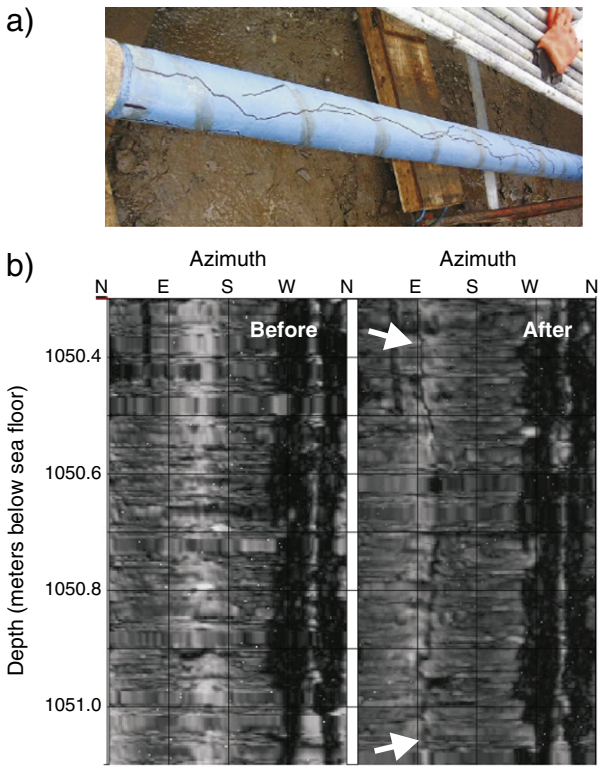

Fig. 16. a) Photograph of an impression packer after removal from the borehole displaying the trace of the induced fracture on the borehole wall. b) Example of borehole televiewer images taken before and after a hydraulic fracture test at a depth of 1050.7 m below the sea floor as part of the ANDRILL South McMurdo Sound drill hole. The induced fracture highlighted between the two white arrows suggests that S_H is directed ESE.
Panel a is an image from Polymetra (2012) used with permission of Polymetra GmBH.

stress tensor (Cornet and Vallette, 1984). Other modifications have sought to include the ability to better sense fracture creation or re-opening using extensometers (Lin and Tommy, 1994), acoustic emissions (Manthei et al., 2003), down hole pumps and pressure sensors (Ito et al., 2006; Thiercelin et al., 1996). Furthermore, electrical imaging of the borehole wall rock surface during the hydraulic fracturing pressurization, shows the most promise for properly interpreting the records (Cornet et al., 2003).

Despite the issues brought up with ambiguities in the interpretation of hydraulic fracturing results, however, the quantitative results produced by this method remain the most trusted.

5.3. Borehole breakouts

Bell and Gough (Bell and Gough, 1979; Gough and Bell, 1981) first observed, using oriented calliper logging information, that the cross-sections of many deep boreholes in Alberta were preferentially elongated in a NW–SE direction. They surmised on the basis of Kirsch's (1898) solutions (Eq. (10)) that those azimuths around a borehole subjected to the maximum concentrated azimuthal compression $\sigma_{\theta\theta}$ occurred at the angle of 90° from the maximum far-field compression S_H (Fig. 4a). Consequently, they suggested that the azimuth of these shear fractures provided clues to the directions of the stresses within the Earth. This was supported by additional field measurements (e.g., Plumb and Hickman, 1985). Today, borehole breakout analyses account for a large majority of the data on in situ stress states. A few photographs of borehole breakouts, or similar features, are shown in Fig. 17 as well as one example of the cross section of a wellbore mapped by the travel times of ultrasonic pulses from an ultrasonic borehole televiewer log.

At first, the actual mechanisms of the formation of the borehole breakouts were not entirely understood. Without this understanding it was not possible to use the breakouts for any quantitative estimation of stress magnitudes; a number of studies were carried out to study the stress concentrations using analytic (Cheatham, 1993; Exadaktylos et al., 2003; Mastin, 1988) or numerical (Zheng et al., 1989) methods and different failure modes (Al-Ajmi and Zimmerman, 2006; Detournay and Roegiers, 1986; Guenot, 1989; Tokar, 1990; Zoback et al., 1985). Indeed, the literature is large and the reader may want to consult the reviews of the topic within both Germanovich and Dyskin (2000) and Haimson (2007).

Borehole breakouts can be produced by different mechanisms as summarized in the photographs taken from laboratory tests in a variety of rock types and a polymer epoxy. Fig. 18a is a classic dog-eared breakout observed in sufficiently stiff and brittle rocks. In this case the breakouts are produced by small extensile buckling that continuously grows similar to those seen in Fig. 17a (see also the examples given by Christiansson (2006) and Germanovich and Dyskin (2000)). Such a progressive failure mechanism was observed in the growth of the large 'breakout' in a mine drift the growth of which was monitored by Martin et al. (1997) in Fig. 17c.

In contrast, shear failure may dominate breakout growth in some softer rocks. Haimson (2007), for example, noted the growth of dilatant shear cracks symmetrical to the S_h springline in tests on a Cordova Cream limestone; similar features may be apparent in hollow cylinder tests in Berea sandstone subjected to a uniform state of radial confining stress (Ewy and Cook, 1990) in Fig. 18b although in this case their azimuth depends on the strength anisotropy of the rock.

On the other hand, compaction banding, too, appears to be responsible for some breakouts produced in highly porous and weak sandstones (Bessinger et al., 1997; Dresen et al., 2010; Haimson, 2007). These unusual 'breakouts' rely on the removal of the sand grains by flow of drilling fluid and produce remarkably linear fractures parallel to the S_H springline (Fig. 18c) and likely contribute to the production of sand through weak formations (Katsman and Haimson, 2011; Katsman et al., 2009).

Finally, elasto-plastic deformations are likely in rocks subjected to creep. An example of a laboratory tests on an epoxy (Tokar, 1990) highlights the ellipse-like yield zone of deformation surrounding a hole in an epoxy block (Fig. 18d). In this case the block was subjected to an anisotropic stress state by applying compression parallel to the borehole axis with the two induced borehole-perpendicular principal stresses resulting from Poisson' ratio expansion against rigid boundaries; as such the stress state is not completely known. The shape of this zone is in qualitative agreement with theoretical predictions that incorporate a Mohr–Coloumb friction law (e.g., Detournay, 1986) and this topic continues to receive attention with different failure mechanisms applied (e.g., Li and Aubertin, 2009; Zhou et al., 2010).

As noted, true breakouts will lengthen the borehole axis in the direction of the S_h spring-line but the borehole retains the original bit diameter gage (i.e., $2a$) perpendicular to this (Fig. 19a). A variety of different kinds of oriented logging tools including oriented callipers (i.e., dip-meters), electrical resistivity imagers, and ultrasonic borehole televiewers are usually used to locate and interpret breakouts as shown in Fig. 20a (see Hurley (2004) and Pöppelreiter et al. (2010) for technical descriptions of the operation of these instruments). More recently, advances in optical imaging technology have allowed the high resolution optical televiewers to be developed (e.g., Fig. 20b) the use of which is limited to air or clean water filled boreholes (e.g., Williams and Johnson, 2004); but there are to date few reports of their use in breakout analysis.

Briefly, oriented calipers have four or more extendable arms that press against the borehole wall and hence provide measures of the borehole diameter at a number of azimuths. The inclination and orientation of the tool is usually provided by a combination of north sensing magnetometers, gyroscopes, and accelerometers. If breakouts exist, the feet of one caliper pair often become ensnared in the breakout gutters. These arms consequently measure at a more or less consistent azimuth diameter greater than the original bit gage while the second orthogonal pair remains at the bit gage (Fig. 19b). As a result, such tools provide both a measure of the depth of a pair of breakouts

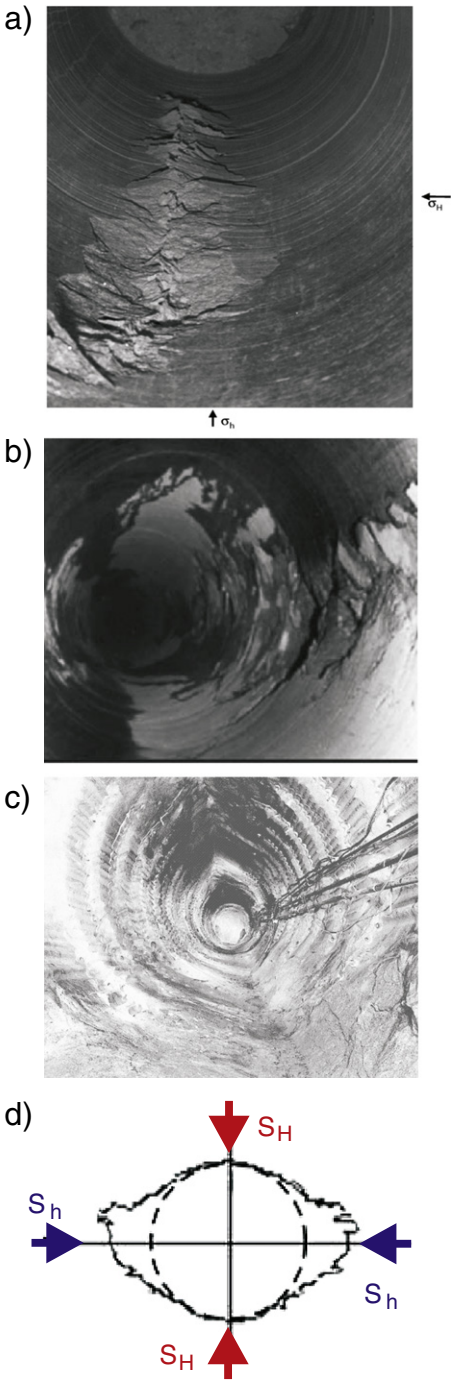

Fig. 17. Photographs of borehole breakouts. a) Incipient extensile buckles on the floor of a borehole drilled in crystalline rock. b) Down-hole borehole breakouts. c) Extensive breakout formation around a circular tunnel excavated in granite. d) Cross-section shape of a breakout in a Hawaiian basalt flow.
Panel a is from Haimson (2007) with permission for reuse granted by Elsevier. Panel b is from Asquith and Krygowski (2004) reprinted with permission of the American Association of Petroleum Geologists under their fair use policy. Panel c is after Martin et al. (1997) reprinted with permission of Elsevier. Panel d is after Morin and Wilkens (2005) reprinted under the Usage Permission policy of the American Geophysical Union.

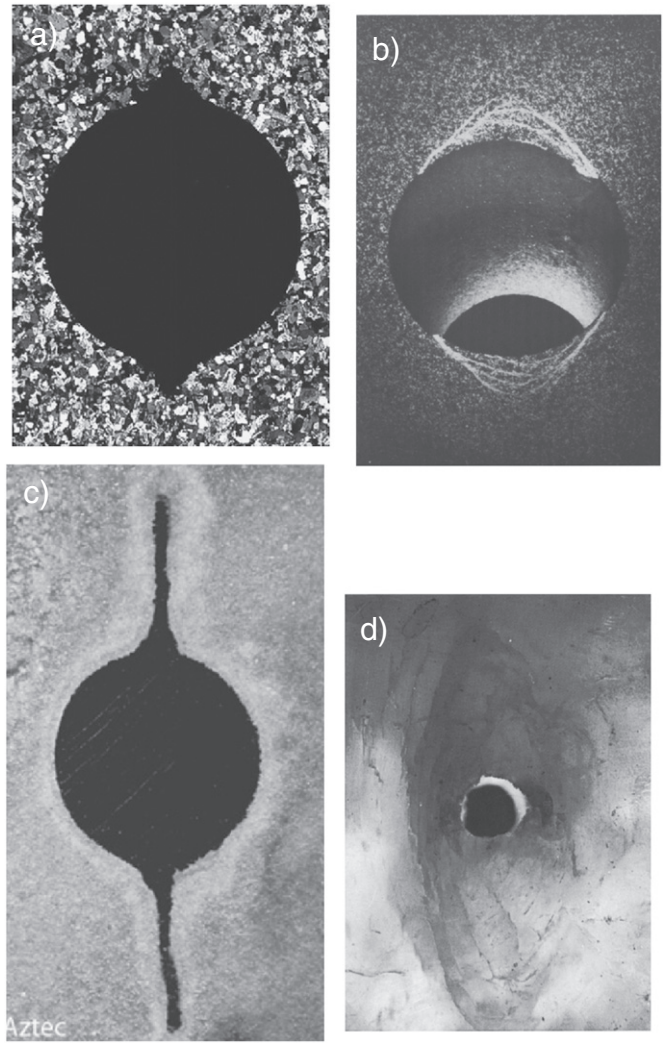

Fig. 18. Examples of laboratory created breakouts from vertical boreholes a) in a Westerly granite cube subject to $S_h = 50$ MPa, $S_V = 60$ MPa, $S_H = 190$ MPa, b) in an anisotropic Berea sandstone hollow cylinder subject to an external confining pressure of 75 MPa, c) in a porous Aztec sandstone subject to $S_h = 20$ MPa, $S_V = 30$ MPa, $S_H = 45$ MPa, and d) a heated *clear* epoxy subject to a triaxial state of stress (stress values unknown). In a) and c) the S_H is directed perpendicular to the springline of the breakouts.
Panel a is from Haimson (2007) with permission to reprint granted by Elsevier. Panel b is from Ewy and Cook (1990) with permission to reprint granted by Elsevier. Panel c is from Haimson (2007) with permission to reprint granted by Elsevier. Panel d is from Tokar (1990) with permission to reprint granted by Elsevier.

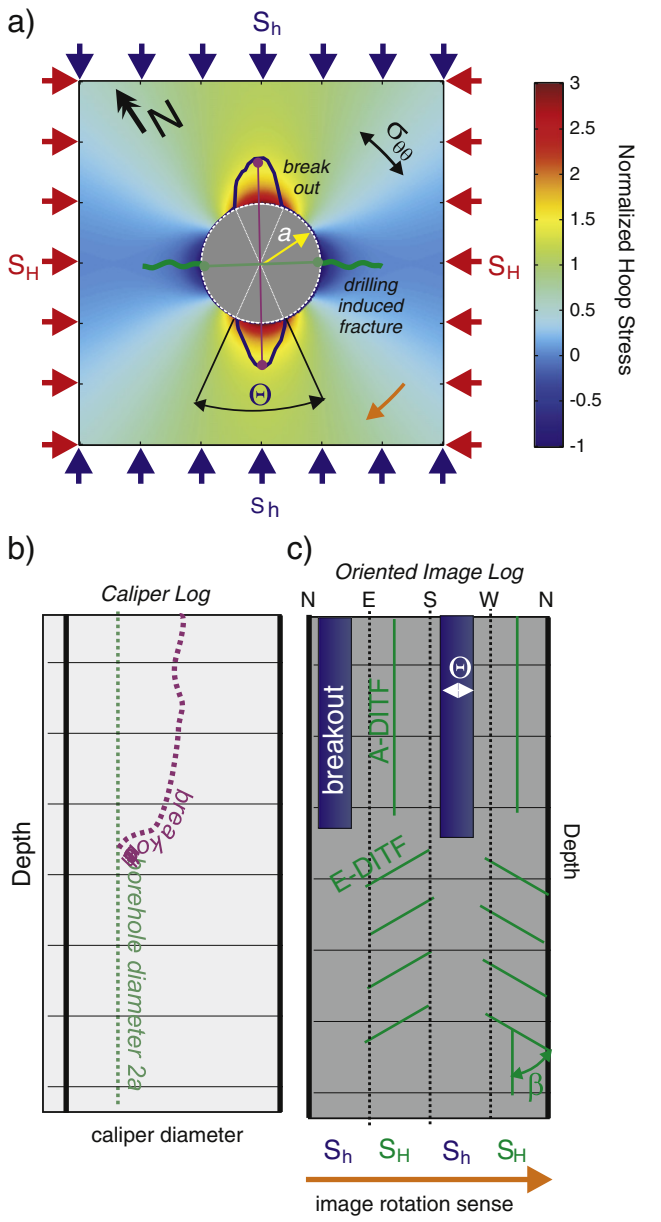

Fig. 19. Cartoons of a) stress induced borehole deformation with the corresponding b) oriented calliper log (e.g., dipmeter), and c) oriented image log. Both axial (A-DITF) and en-echelon (E-DITF) drilling induced tensile fractures (green) and borehole breakouts (blue) that are parallel and perpendicular to the S_H spring-line, respectively.

and their orientation that falling along the S_h springline provides information on the horizontal stress directions.

Imaging tools provide a 360° view of the borehole wall rock (Fig. 19c) that allows for additional measurements of breakout geometry, such as the breakout width Θ, to be estimated. This information has been used to constrain the magnitudes of the horizontal stresses by various authors (e.g., Zoback et al., 2003) under the assumptions i) that the borehole width does not change as the breakout progressively deepens and ii) that the edge of the breakout corresponds to the azimuth at which the stress state first exceeds the rock strength. Later laboratory tests (Haimson and Herrick, 1986) were consistent with this suggestion. Accordingly, and further assuming a Mohr–Coulomb failure criteria (Eq. (20)) S_H may be estimated as (Barton et al., 1988)

$$S_H = \frac{UCS + \Delta\sigma_{\theta\theta} - S_h(1-2\cos(\Theta))}{1+2\cos(\Theta)} \tag{25}$$

where *UCS* is the unconfined compressive strength that, ideally, could be determined by finding stress at which a laterally unconfined and uniaxially loaded sample fails. *UCS* is related to the cohesion *C* allowing the Mohr–Coulomb failure condition (Eq. (20)) to be alternatively written as

$$\tau = \sigma\mu + \frac{UCS}{2\left[\left(\mu^2+1\right)^{1/2}+\mu\right]}. \tag{26}$$

One problem with the application of Eq. (25) is that S_H depends on the unconfined *UCS* which is often not well known as it must be determined in laboratory measurements on rocks. Properly determining *UCS* necessitates a suite of tests on the rock to produce the shear failure envelope. Unfortunately, there is rarely sufficient core available to carry out these tests and instead proxies based on lithological knowledge (Batir et al., 2012) and geophysical logs are found (see Chang et al., 2006; Sharma et al., 2010).

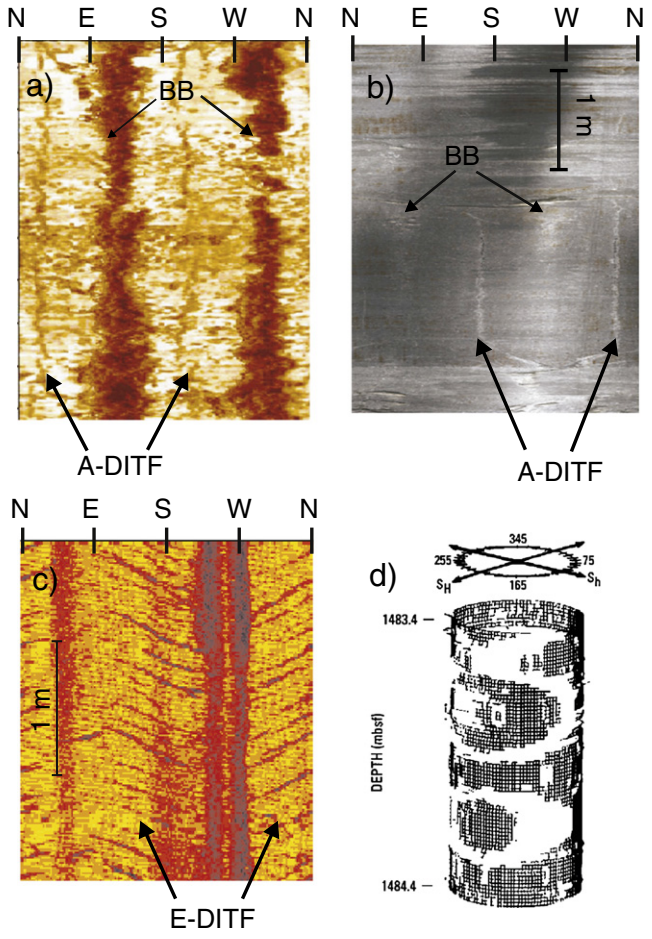

Fig. 20. Examples of drilling induced tensile fractures (DITF) and borehole breakouts (BB) from a) an ultrasonic borehole televiewer image containing both axial A-DITF and borehole breakouts, b) an optical televiewer image of axial A-DITF with incipient breakouts, c) transverse en-echelon E-DITF observed in electrical image log, and d) oval fractures observed in ultrasonic televiewer images in basalt.
Panel a is after Zoback et al. (2003) with permission to reprint granted by Elsevier. Panel b is from Lucier et al. (2009) with permission to reprint granted by Elsevier. Panel d is after Valley and Evans (2009) with permission to reuse granted by Springer. Panel d is after Morin and Wilkens (2005) with permission to reuse granted by the American Geophysical Union.

Work following from this has employed failure criteria that depend on the value of the intermediate state of stress such as the theoretical Weibol–Cook criterion (Vernik and Zoback, 1992), the empirical Mogi criterion (Haimson and Chang, 2002), or a combined Mises–Schleicher–Drucker–Prager criterion (Aubertin et al., 2000; Simon and Labrie, 2012).

It needs to be noted, however, that the use of breakout widths to constrain stress magnitudes remains controversial; Detournay and Roegiers (1986), for example, point out a number of possible deficiencies ranging from geometrical kinematics to lack of precise knowledge of the deformation mechanisms active. For example, repeated measurements of the borehole cross-sections in different boreholes drilled as part of the NanTroSEIZE project demonstrate that the observed breakout widths increase with time (Moore et al., 2011) within the weak sediments logged. Also, Martin et al. (1997) measured the growth of breakout depth and width in a tunnel through granite and granodiorite over a period of several months.

5.4. Drilling induced tensile fractures

Borehole breakouts are not the only type of stress induced damage seen on the walls of boreholes; a variety of drilling induced tensile fractures (DITF) and shear fractures are also observed (Aadnoy and Bell, 1998). The simplest of these are axial-DITF (A-DITF) in Fig. 20a–b with more complex sets appearing in an en-echelon or chevron pattern (E-DITF) in Fig. 20c.

The axial and en-echelon fractures are interpreted to occur under conditions in which the principal stresses are aligned or oblique to the borehole axis, respectively. In some cases, they could be inadvertent hydraulic fractures produced by the wellbore static or transient (e.g., swabbing) pressure of the drilling fluids much as described above for hydraulic fracture initiation (Aadnoy, 1990). They could also result from thermal disturbances caused by cooler temperatures of the drilling fluid. Or, they could result from concentrated tensional stress at the borehole wall according to Kirsch's solutions (Eq. (10)) (Brudy and Zoback, 1999).

Although these appear to be tensile features and they appear at those azimuths in tension along the borehole wall they have also been interpreted as natural fractures that have slipped due to the tension and have been referred to as drilling-enhanced fractures (e.g., Barton and Zoback, 2002; Barton et al., 2009). Regardless, these fractures provide the direction of S_H and may provide information to constrain stress magnitudes (Aadnoy, 1990; Brudy and Zoback, 1993; Djurhuus and Aadnoy, 2003; Hayashi et al., 2003; Nelson et al., 2005; Okabe et al., 1998; Peska and Zoback, 1995; Schmitt, 1993; Valley and Evans, 2009) if the wellbore fluid pressures and temperatures are known in a manner analogous to the use of hydraulic fracture data.

Observations of drilling induced fractures are useful in that they can be used to further constrain the in situ stress magnitudes. The formation of A-DITF is essentially the same as for intentional hydraulic fracturing (Eq. (22)). Consequently, careful assessment of the down hole fluid mud pressures together with independent knowledge of S_h can provide an estimate of S_H (Wiprut and Zoback, 2000).

Similarly, interpretation of the E-DITF requires that the angle β of their trace with respect to the borehole axis be measurable (Aadnoy and Bell, 1998). In this case, one must consider the full state of stress at the borehole wall as generated by the in situ stresses (Eq. (11)) as adjusted by the borehole boundary conditions (Eq. (18)). One expects the tensile fracture to open in parallel to the minimum principal compression σ_3 with the angle of the fracture β

$$\beta = \arccos\left[\frac{\tau_{\theta z}}{\left[(\sigma_{\theta\theta}-\sigma_3)^2+\tau_{\theta z}^2\right]^{1/2}}\right] \tag{27}$$

where

$$\sigma_3 = \frac{\sigma_{\theta\theta}+\sigma_{zz}}{2} - \frac{\sqrt{(\sigma_{\theta\theta}-\sigma_{zz})^2+4\tau_{\theta z}^2}}{2} \tag{28}$$

as first derived by Aadnoy (1990). More recently, Thorsen (2011) has developed linearized failure criteria along similar lines.

Morin (1990) observed oval shaped fractures on the borehole wall (Fig. 20d) that they interpreted based on an analytical analysis to be produced by a combination of the far-field and thermal stress concentrations. Similar fractures were recently reported in image logs from the Coso geothermal field, Nevada (Davatzes and Hickman, 2010). The source of such fractures requires further investigation.

6. Stress indications from core studies

6.1. Drilling induced core fractures

Cores retrieved from the borehole are also damaged by concentrations of the in situ stresses leading to damage and macroscopic fracturing. Drilling induced core fractures (DICF) are created during coring operations, their shapes and spacing suggests that they too

contain clues to in situ stress directions and magnitudes. The types of core fractures observed (Figs. 21, 22) have been classified (Hakala, 1999; Kulander et al., 1990; Venet et al., 1990) as ranging from convex through flat to concave, the axial symmetry of which suggests relatively uniform horizontal stresses, and saddle-shaped through to petal-centerline the asymmetry of which indicates anisotropic far-field stresses (Fig. 23). In many cases, particularly where borehole stability is an issue and geophysical logging or hydraulic fracturing becomes impossible, these core fractures may be the only information available on the in situ state of stress; understanding the relationships between their shapes and spacings has been a goal of many workers.

Despite the fact that rocks are complex materials, such fractures are remarkably uniform along a core in both spacing and shape as may be seen in the photographs of Fig. 21. Additional excellent examples of core disks with a variety of thicknesses may be found in Lim and Martin (2010). Further, the morphology of these fractures seems to show that they are purely tensile features; this is supported by fractographic analyses of the fracture surfaces (Bankwitz and Bankwitz, 1997, 2000; Kulander et al., 1990) (Fig. 22). Li and Schmitt (1998) demonstrated that the point of fracture initiation is an important additional piece of information. Since the state of stress in the Earth is almost always compressive the occurrence of tensile fractures suggests that they are produced by concentration of the stresses by the geometry at the bottom of the borehole.

The stress concentrations at the bottom-hole and near the core stub are not as easily obtained as the axisymmetric stresses away from any ends of a long borehole (Eq. (11)). The asymmetric and three dimensional bottom-hole cannot be described in simple closed form equations (e.g., Coates and Yu, 1970), and aside from some empirical measurements (Galle and Wilhoit, 1962) numerical approaches have been the method of choice in attempting to better understand the bottom-hole stress concentrations. Hocking (1976) provides a comprehensive review of the experimental and numerical work up to the mid-1970s. Since then, the problem has received continued attention with application to failure and damage at the ends of tunnels and boreholes (e.g., Diederichs et al., 2004; Eberhardt, 2001; Ito et al., 1998; Rumzan and Schmitt, 2001) and for overcoring techniques (Kang et al., 2006; Wang and Wong, 1987). However, much of the focus of the overcoring/undercoring community lies in finding sets of experimental geometry-dependent stress concentration factors and the work is usually not directly transferrable to the study of core damage.

Before continuing, it is useful to better define the geometry of drilling induced core fractures (DICF). Different types of coring bits are used for various purposes in the petroleum, mining, and nuclear waste industries (Fig. 24). The bit essentially grinds away the material around the central stub or pedestal of the core materials. The shape and width of the cut out slot, or kerf, of course depend on the type of coring bit employed, and this must influence the final distribution of the stresses. Further, as might be inferred by the photographs in Fig. 21, the core fractures are more or less uniformly spaced; and this suggests that the core stub length also influences stress concentrations.

This core–stub geometry (Fig. 24c) is more complex than a simple flat ended borehole and workers have been forced towards numerical approaches in attempting to understand such fractures. The finite element method has been used in most of these studies (Dyke, 1989; Hakala, 1999; Kaga et al., 2003; Li and Schmitt, 1997a, 1997b, 1998; Lim and Martin, 2010; Lim et al., 2006; Matsuki et al., 2003, 2004; Sugawara et al., 1978; Venet, 1993; Venet et al., 1990). One exception is the study of Gorodkov et al. (2006) which used a discrete particle approach to look at the damage produced in a core stub of granular material during coring.

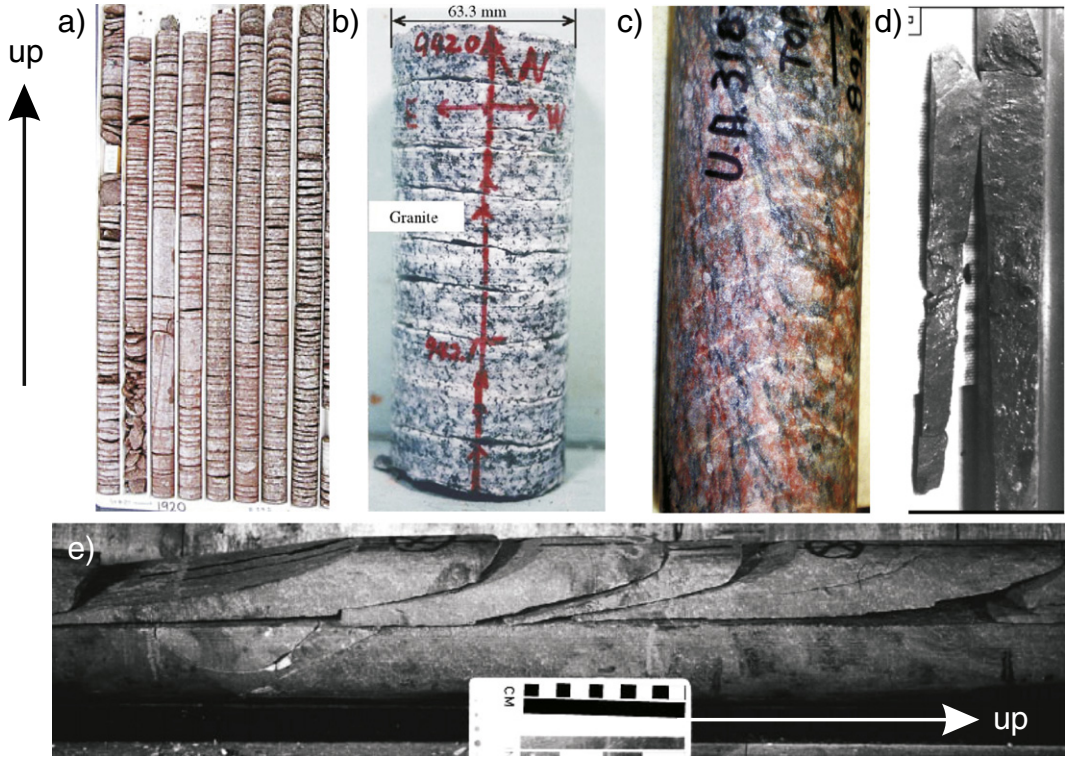

Fig. 21. Examples of drilling induced core fracture phenomena. a) Series of flat core disks along length of core. b) Series of uniformly spaced concave saddle shaped disks from a depth of 942 m from a vertical borehole at Sakuma, Shizuoka prefecture, Japan. c) Petal fractures in metamorphic rock from the Canadian shield in Alberta. d) Example of core-edge fractures. e) Series of petal-centerline fractures in West Texas limestone core.
Panel a is after Bunger (2010) with permission for reuse granted by Springer. Panel b is from Kang et al. (2006) with permission for reuse granted by Elsevier. Panel c is a personal photograph of Schmitt. Panel d is from Wilson and Paulsen (2000) with permission for reuse granted by the journal Terra Antartica. Panel e is from http://www.naturalfractures.com/ used with the permission of Dr. A. Lacazette.

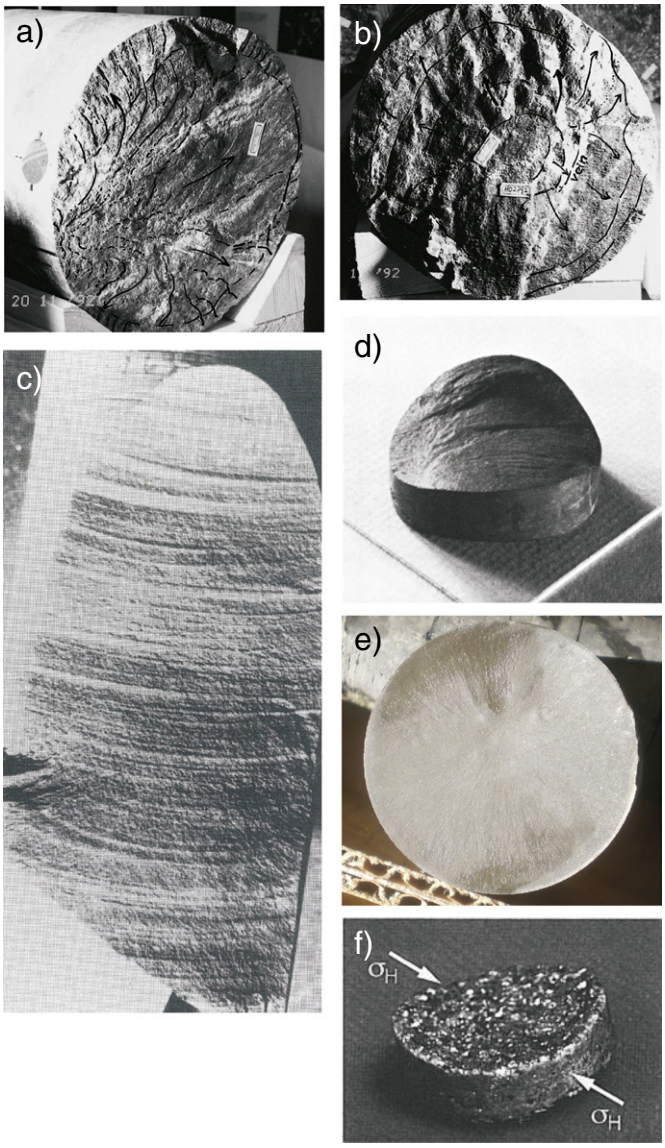

Fig. 22. Examples of drilling induced core fracture surfaces showing tensile nature. a) Disk fracture initiating from core edge, b) disk fracture initiating from core axis, c) petal-centerline fracture initiating at core edge, d) convex saddle shaped core disk, e) weakly concave disk fracture with fracture initiation point near center of core in brittle shale, f) concave saddle shaped disk produced in laboratory experiments on Westerly granite.
Panel a is from Bankwitz and Bankwitz (1997) with permission for reuse granted by Springer. Panel b is from Bankwitz and Bankwitz (1997) with permission for reuse granted by Springer. Panel c is from Kulander et al. (1990) with permission for reuse under the American Association of Petroleum Geologists' fair use policy. Panel d is from Paillet and Kim (1987) with permission for use granted by the American Geophysical Union. Panel e is a photo courtesy of D.R. Schmitt. Panel f is from Song and Haimson (1999) used with permission of the American Rock Mechanics Association.

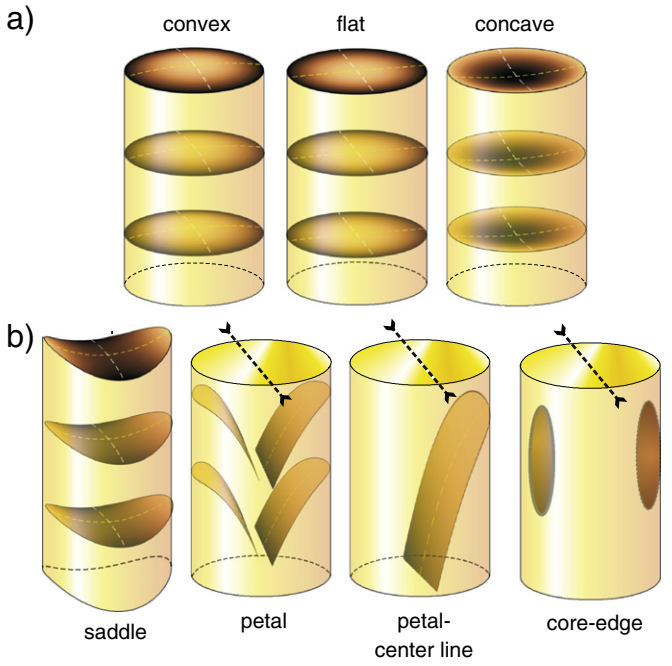

Fig. 23. Classification of differing types of drilling induced core fractures from a vertical borehole. a) Disk fractures formed under a uniform state of horizontal stress. b) Saddle-shaped, petal, and core edge fractures formed under an anisotropic state of stress perpendicular to the borehole axis. The strike of these fractures (shown by dashed lines) indicates the direction of S_H.

Experimental studies of such fractures remain quite limited (Jaeger and Cook, 1963; Obert and Stephenson, 1965). More recently Haimson and coworkers (Haimson and Lee, 1995; Song and Haimson, 1999) carried out core-drilling experiments on blocks of rock subjected to a variety of true triaxial states of stress. They showed that the thickness of the disks depended on the magnitudes of the horizontal stresses and for the first time experimentally demonstrated that the strike of the 'troughs' of the fractures are parallel to S_H for an anisotropic state of horizontal stress (Fig. 22f).

One issue in attempting to predict what form the DICF will take is that the criterion for both fracture initiation and propagation is not necessarily well understood. Predicting the path that a fracture will propagate remains an unsolved problem even today (see Pook, 2010). However, it is instructive to look at what kinds of criteria have been employed. Dyke (1989) attempted to localize the fracture trajectory on the basis of strain energy arguments. Li and Schmitt (1998) carried out 3D FEM models on a variety of core stub geometries and used a simple maximum tensile stress failure criterion to both initiate and propagate the tensional fractures. This approach was also adopted by Hakala (1999). Matsuki et al. (2004) carried out extensive finite element modeling for a variety of core stub lengths subjected to general states of far-field stresses. Using reasonable assumptions on the uniformity and direction of stress within the stub they developed a set of 'critical tensile stress' criteria that allow estimation of the full stress field. Bunger (2010) has applied Matsuki et al.'s (2004) criterion for statistical evaluation of a large number of core disks from a South African borehole. Lim and Martin (2010) applied a fracture mechanics approach that yields disk surfaces in agreement with field observations.

Most recently, Zhang (2011) made high element density 3D FEM calculations of the stresses around a borehole containing stubs. As with earlier modeling, high *pure tensional* stresses are generated in and around the core stub (Fig. 25). This extended the 2D fracture propagation models of Li and Schmitt (1998) to a 3D fracture propagation scheme. This model was able to replicate all of the shapes in Fig. 21 with the exception of the core edge fractures. As in Li and Schmitt (1998), the modeling allows for a general interpretation of the fracture shapes to assist in constraining the faulting environment encountered.

6.2. Core damage based methods

To complete this section, we mention two related core-based techniques that attempt to extract additional stress information from the retrieved cores.

The first employs the concept that rocks, like many advanced materials, retain some 'memory' of the stresses they had experienced.

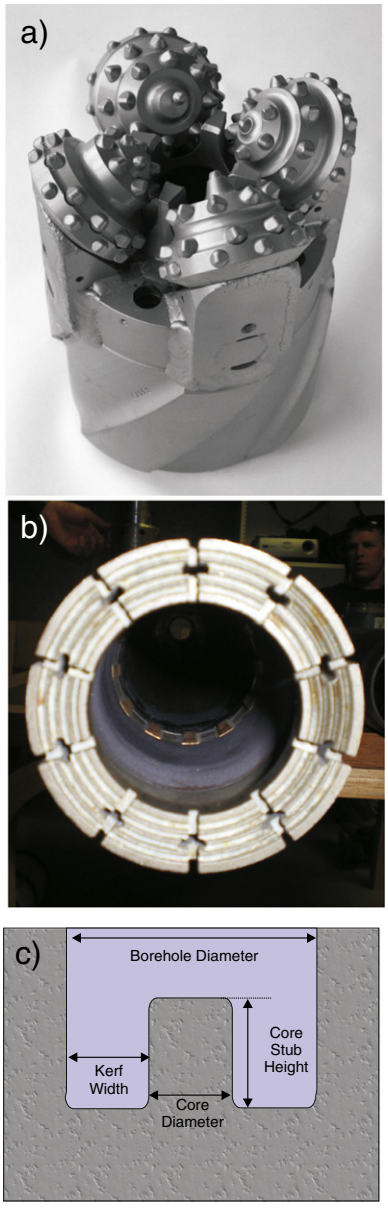

Fig. 24. Types of coring bits. a) Rotary tri-cone core bit produces 58.7 mm diameter core, b) typical PQ-dimension diamond impregnated coring bit with 85.09 mm diameter core, c) side view through the borehole bottom showing the core stub.
Panel a is a photo from http://www-odp.tamu.edu/publications/tnotes/tn31/title.htm with permission for use granted from ODP Publication Services. Panel b is a photo courtesy of D.R. Schmitt.

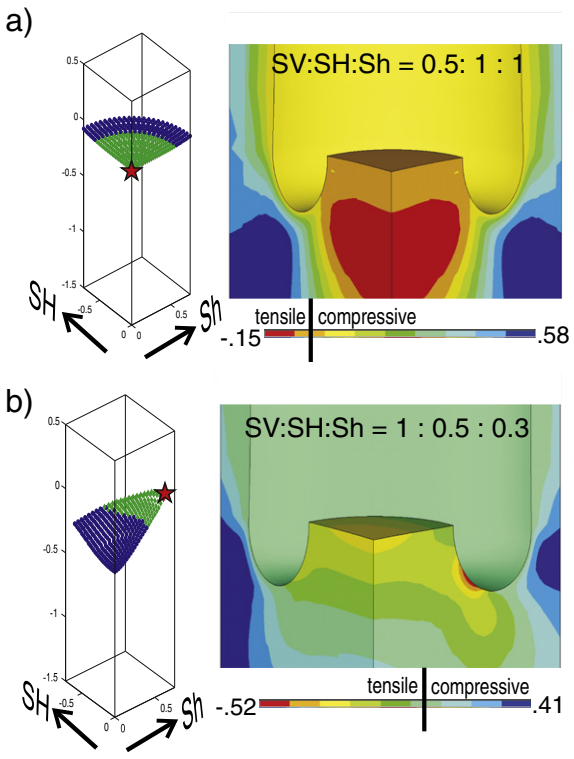

Fig. 25. Examples of finite element stress calculations. Left panels show the resulting fracture shape in 3-dimensions with green surfaces representing zones with tensional stress and blue surfaces representing extension of the fracture into compressional zones. Right panels show the values of the most tensile principle stress as normalized with respect to the maximum applied compression. a) Case of uniform horizontal stresses $S_h = S_H = 2S_V$ displays large zone under pure tension centered on borehole axis (right image). A concave disk fracture initiates at the point of the greatest tension. b) Case of unequal horizontal stresses $S_V = 2S_H = 3.3S_h$ displays high tension at the S_h azimuth with a formation of a petal fracture that initiates at the core surface.
After Zhang (2011).

Here, the Kaiser effect (Kaiser, 1950; Li and Nordlund, 1993) consists of monitoring the acoustic emissions from a previously stressed material while it is again stressed. This method presumes that no new crack damage is initiated in the sample, with the result that there are no acoustic emissions detected, until the sample is stressed past its original in situ stress state. At this point new damage is initiated with acoustic emissions produced. Yamamoto (2009) also uses similar ideas but by carefully measuring strains during reloading of a rock sample to estimate stress magnitudes.

The second method is called 'anelastic strain recovery' (ASR) (Engelder, 1984; Lin et al., 2006; Matsuki, 2008; Matsuki and Takeuchi, 1993; Wolter and Berckhemer, 1989). The underlying premise of this technique is that rocks are viscoelastic materials. As such, their deformation is time dependent; and as the initial stress relaxes in the sample it creeps in response. Therefore, workers monitor the creep behavior of the core with time immediately upon recovery from the Earth. The 3D deformation is then inverted via a model of viscoelastic behavior to provide an estimate of the stress directions and magnitudes.

It is likely that both the Kaiser effect and ASR are affected by the damage induced by the high tensile stresses experienced during coring as demonstrated for example in Fig. 25. This tension is likely to produce micro-cracking of the sample even if no visible macroscopic drilling induced fracture is seen. Additional work needs to resolve the relationship between these effects and coring induced damage. Further, it is interesting to consider the possibility of relationships between induced fractures in the core and those seen in the borehole wall (Fig. 20) as the core fractures may provide additional information to support the borehole observations (Davatzes and Hickman, 2010).

Although the core based techniques do show promise, they still require that a dedicated practitioner carry out the measurements. More research into the validity and ranges of suitability of these techniques is necessary.

7. Concluding remarks

This review has focused primarily on providing a basic understanding of many of the techniques used to obtain the directions and magnitudes of stresses from deep boreholes. No single technique discussed here provides the 'magic bullet' to determine the complete state of in situ stress. As such, current practices focus on obtaining as much information as possible from a variety of indicators that include advanced acoustic logging, borehole breakouts, drilling induced tensile fractures, hydraulic fractures and leak off tests, and drilling induced core fractures.

Again, given the focus here on fundamentals there is insufficient space to show actual applications. There are a number of good examples of this multiple approach most of which come from scientific drilling projects that often include detailed borehole and core logging and, more rarely, hydraulic mini-frac testing. The deep German KTB project provided many opportunities for stress constraint using breakouts, drilling induced fractures, and hydraulic fracturing (Brudy et al., 1997; Haimson and Chang, 2002), core disking (Bankwitz and Bankwitz, 2000), and anelastic strain recovery (Wolter and Berckhemer, 1990). Since then, expanded studies have occurred in the pilot and main holes of the San Andreas Fault Observatory at Depth (SAFOD) project (Boness and Zoback, 2006; Hickman and Zoback, 2004) and at the Chelungpu fault, Taiwan (Haimson, 2010a; Haimson et al., 2010; Lin et al., 2010; Zhang and Roegiers, 2010), to name only a few. The reader can find examples of the integration of the various methods by studying the protocols and reasoning used to produce stress profiles in those examples. Unfortunately, some of the best work arising from the deep marine drilling for the petroleum industry remains proprietary.

Significant progress has been made in stress indication and measurement particularly since it was realized that the patterns of borehole and core damage are highly diagnostic of stress states. However, much remains to be done. Obtaining true measures of the full three dimensional stress tensor is still elusive. Furthermore, much future drilling will be from deviated or horizontal boreholes and more can be done to understand how they will fail or how hydraulic fractures will grow from them (Haimson, 2010b). These issues will be of particular concern for unconventional hydrocarbon production where there are hints that stress heterogeneity or fracturing induced stress changes are important (Warpinski, 1989). Finally, a good understanding of the relationship between stresses and the material physical properties will be necessary to reduce the current limits of stress measurements and their interpretations.

Acknowledgments

This work is supported by the Canada Research Chairs and NSERC. This paper honors Prof. T.J. Ahrens (d. December, 2010) for starting and Prof. D.I. Gough (d. March, 2011) for continuing to inspire Schmitt's interest in crustal stress measurement. Q. Jia's care in reviewing the equations is greatly appreciated.

References

Aadnoy, B.S., 1990. In-situ stress directions from borehole fracture traces. Journal of Petroleum Science and Engineering 4, 143–153.
Aadnoy, B.S., Angellolsen, F., 1995. Some effects of ellipticity on the fracturing and collapse behavior of a borehole. International Journal of Rock Mechanics and Mining Sciences 32, 621–627.
Aadnoy, B.S., Bell, J.S., 1998. Classification of drilling induced fractures and their relationship to in situ stress directions. The Log Analyst, pp. 27–42.
Abousleiman, Y.N., Chen, S.L., 2010. Poromechanics response of an inclined borehole subject to in-situ stress and finite length fluid discharge. Journal of Mechanics of Materials and Structures 5, 47–66.
Adams, J., 1982. Stress-relief buckles in the Mcfarland Quarry, Ottawa. Canadian Journal of Earth Sciences 19, 1883–1887.
Adams, L.H., Williamson, E.D., 1923. On the compressibility of minerals and rocks at high pressures. Journal of the Franklin Institute 195, 475–529.
Al-Ajmi, A.M., Zimmerman, R.W., 2006. Stability analysis of vertical boreholes using the Mogi–Coulomb failure criterion. International Journal of Rock Mechanics and Mining Sciences 43, 1200–1211.
Amadei, B., 1983. Rock Anisotropy and the Theory of Stress Measurements. Springer-Verlag, Berlin.
Amadei, B., Stephannson, O., 1997. Rock Stress and its Measurement. Chapman and Hall, New York.
Amadei, B., Swolfs, H.S., Savage, W.Z., 1988. Gravity-induced stresses in stratified rock masses. Rock Mechanics and Rock Engineering 21, 1–20.
Anderson, E.M., 1951. The Dynamics of Faulting and Dyke Formation with Applications to Britain, 2nd ed. Oliver and Boyd, London and Edinburgh.
Ashraf Mohammed, A., Abousleiman, Y.N., 2008. Acoustic measurement and calibration of in situ stress anisotropy around a wellbore. SPE Annual Technical Conference and Exhibition. Society of Petroleum Engineers, Denver, Colorado, USA.
Ask, D., Cornet, F.H., Fontbonne, F., Nilsson, T., Jonsson, L., Ask, M.V.S., 2009. A quadruple packer tool for conducting hydraulic stress measurements in mines and other high stress settings. International Journal of Rock Mechanics and Mining Sciences 46, 1097–1102.
Asquith, G., Krygowski, D., 2004. Basic Well Log Analysis. AAPG, Tulsa.
Aubertin, M., Li, L., Simon, R., 2000. A multiaxial stress criterion for short- and long-term strength of isotropic rock media. International Journal of Rock Mechanics and Mining Sciences 37, 1169–1193.
Balland, C., Renaud, V., 2009. High-resolution velocity field imaging around a borehole: excavation-damaged zone characterization. Geophysics 74, E223–E232.
Bankwitz, P., Bankwitz, E., 1997. Fractographic features on joints in KTB drill cores as indicators of the contemporary stress orientation. Geologische Rundschau 86, S34–S44.
Bankwitz, P., Bankwitz, E., 2000. Drilling-induced fracturing processes and the evidence for the in situ stress field (KTB drilling site, NE Bavaria). Neues Jahrbuch Fur Geologie Und Palaontologie-Abhandlungen 218, 85–127.
Barton, C.A., Zoback, M.D., 2002. Discrimination of natural fractures from drilling-induced wellbore failures in wellbore image data—implications for reservoir permeability. SPE Reservoir Evaluation and Engineering 5, 249–254.
Barton, C.A., Zoback, M.D., Burns, K.L., 1988. In situ stress orientation and magnitude at the Fenton geothermal site, New Mexico, determined from wellbore breakouts. Geophysical Research Letters 15, 467–470.
Barton, C., Moos, D., Tezuka, K., 2009. Geomechanical wellbore imaging: implications for reservoir fracture permeability. AAPG Bulletin 93, 1551–1569.
Batir, J., Davatzes, N., Asmundsson, R., 2012. Preliminary model of fracture and stress state in the Hellisheidi geothermal field, Hengill volcanic system, Iceland. Thirty-Seventh Workshop on Geothermal Reservoir Engineering. Stanford University, Stanford, California, p. 18.
Batista, M., 2010. On the stress concentration around a hole in an infinite plate subject to a uniform load at infinity. International Journal of Mechanical Sciences 53, 254–261.
Bell, J.S., 1985. Offset boreholes in the rocky mountains of Alberta, Canada. Geology 13, 734–737.
Bell, J.S., Gough, D.I., 1979. Northeast–southwest compressive stress in Alberta — evidence from oil-wells. Earth and Planetary Science Letters 45, 475–482.
Berg, C.A., 1965. Deformation of fine cracks under high pressure and shear. Journal of Geophysical Research 70, 3447-&.
Bessinger, B.A., Liu, Z., Cook, N.G.W., Myer, L.R., 1997. A new fracturing mechanism for granular media. Geophysical Research Letters 24, 2605–2608.
Birch, F., 1961. Velocity of compressional waves in rocks to 10 kilobars, part 2. Journal of Geophysical Research 66, 2199-&.
Boness, N.L., Zoback, M.D., 2006. A multiscale study of the mechanisms controlling shear velocity anisotropy in the San Andreas Fault Observatory at Depth. Geophysics 71, F131–F146.
Bott, M.H.P., 1993. Modeling the plate-driving mechanism. Journal of the Geological Society 150, 941–951.
Bredehoeft, J.D., Wolff, R.G., Keys, W.S., Shuter, E., 1976. Hydraulic fracturing to determine regional in situ stress field, Piceance Basin, Colorado. Geological Society of America Bulletin 87, 250–258.
Brudy, M., Zoback, M.D., 1993. Compressive and tensile failure of boreholes arbitrarily-inclined to principal stress axes — application to the KTB boreholes, Germany. International Journal of Rock Mechanics and Mining Sciences 30, 1035–1038.
Brudy, M., Zoback, M.D., 1999. Drilling-induced tensile wall-fractures: implications for determination of in-situ stress orientation and magnitude. International Journal of Rock Mechanics and Mining Sciences 36, 191–215.
Brudy, M., Zoback, M.D., Fuchs, K., Rummel, F., Baumgartner, J., 1997. Estimation of the complete stress tensor to 8 km depth in the KTB scientific drill holes: implications for crustal strength. Journal of Geophysical Research—Solid Earth 102, 18453–18475.
Bunger, A.P., 2010. Stochastic analysis of core discing for estimation of in situ stress. Rock Mechanics and Rock Engineering 43, 275–286.
Chang, C.D., Zoback, M.D., Khaksar, A., 2006. Empirical relations between rock strength and physical properties in sedimentary rocks. Journal of Petroleum Science and Engineering 51, 223–237.
Cheatham, J.B., 1993. A new hypothesis to explain stability of borehole breakouts. International Journal of Rock Mechanics and Mining Sciences 30, 1095–1101.
Chen, Z.R., 2011. Poroelastic model for induced stresses and deformations in hydrocarbon and geothermal reservoirs. Journal of Petroleum Science and Engineering 80, 41–52.
Chin, L.Y., Raghavan, R., Thomas, L.K., 2000. Fully coupled analysis of well responses in stress-sensitive reservoirs. SPE Reservoir Evaluation and Engineering 3.
Christiansson, R., 2006. The latest developments for in-situ rock stress measuring techniques. In: Lu, M., Li, C., Kjorholt, H., Dahle, H. (Eds.), In-situ Rock Stress. Taylor & Francis, Trondheim, pp. 3–10.
Ciz, R., Shapiro, S.A., 2009. Stress-dependent anisotropy in transversely isotropic rocks: comparison between theory and laboratory experiment on shale. Geophysics 74, D7–D12.
Coates, D.F., Yu, Y.S., 1970. A note on stress concentrations at end of a cylindrical hole. International Journal of Rock Mechanics and Mining Sciences 7, 583–588.
Colmenares, L.B., Zoback, M.D., 2002. A statistical evaluation of intact rock failure criteria constrained by polyaxial test data for five different rocks. International Journal of Rock Mechanics and Mining Sciences 39, 695–729.
Cornet, F.H., 1993. 12. Stresses in rock and rock masses: principles, practice, and projects. In: Hudson, J.A. (Ed.), Comprehensive Rock Engineering. Pergamon Press, Oxford, pp. 297–327.
Cornet, F.H., Vallette, B., 1984. In situ stress determination from hydraulic injection test data. Journal of Geophysical Research 89, 11527–11537.

Cornet, F.H., Doan, M.L., Fontbonne, F., 2003. Electrical imaging and hydraulic testing for a complete stress determination. International Journal of Rock Mechanics and Mining Sciences 40, 1225–1241.
Corthesy, R., He, G., Gill, D.E., Leite, M.H., 1999. A stress calculation model for the 3d borehole slotter. International Journal of Rock Mechanics and Mining Sciences 36, 493–508.
Daneshy, A.A., 1971. True and apparent direction of hydraulic fractures paper number 3226. Drilling and Rock Mechanics Conference, Austin, pp. 149–163.
Davatzes, N., Hickman, S.H., 2010. Stress, fracture, and fluid-flow analysis using acoustic and electrical image logs in hot fractured granites of the Coso geothermal field, California, U.S.A. In: Pöppelreiter, M., Garcia-Carballido, C., Kraaijveld, M. (Eds.), Dipmeter and Borehole Image Log Technology. American Association of Petroleum Geologists, Tulsa, pp. 259–293.
Detournay, E., 1986. An approximate statical solution of the elastoplastic interface for the problem of Galin with a cohesive-frictional material. International Journal of Solids and Structures 22, 1435–1454.
Detournay, E., Cheng, A.H.D., 1988. Poroelastic response of a borehole in a non-hydrostatic stress-field. International Journal of Rock Mechanics and Mining Sciences & Geomechanics Abstracts 25, 171–182.
Detournay, E., Roegiers, J.C., 1986. Well bore breakouts and in situ stress — comment. Journal of Geophysical Research—Solid Earth and Planets 91, 14161–14162.
Diederichs, M.S., Kaiser, P.K., Eberhardt, E., 2004. Damage initiation and propagation in hard rock during tunnelling and the influence of near-face stress rotation. International Journal of Rock Mechanics and Mining Sciences 41, 785–812.
Djurhuus, J., Aadnoy, B.S., 2003. In situ, stress state from inversion of fracturing data from oil wells and borehole image logs. Journal of Petroleum Science and Engineering 38, 121–130.
Dresen, G., Stanchits, S., Rybacki, E., 2010. Borehole breakout evolution through acoustic emission location analysis. International Journal of Rock Mechanics and Mining Sciences 47, 426–435.
Dyke, C., 1989. Core Disking: Its Potential as an Indicator of Principal Stress Directions. In: Maury, V., Formaintraux, D. (Eds.), Balkema, Rotterdam, pp. 1057–1064.
Eberhardt, E., 2001. Numerical modelling of three-dimension stress rotation ahead of an advancing tunnel face. International Journal of Rock Mechanics and Mining Sciences 38, 499–518.
Edwards, R.H., 1951. Stress concentrations around spheroidal inclusions and cavities. Journal of Energy Resources Technology—Transactions of the ASME 18, 19–30.
Ellefsen, K.J., Cheng, C.H., Toksoz, M.N., 1991. Effects of anisotropy upon the normal-modes in a borehole. Journal of the Acoustical Society of America 89, 2597–2616.
Engelder, T., 1984. The time-dependent strain relaxation of Algerie granite. International Journal of Rock Mechanics and Mining Sciences 21, 63–73.
Engelder, T., Geiser, P., 1980. On the use of regional joint sets as trajectories of paleostress fields during the development of the Appalachian Plateau, New-York. Journal of Geophysical Research 85, 6319–6341.
Esmersoy, C., Koster, K., Williams, M., Boyd, A., Kane, M., 1994. Dipole shear anisotropy logging. SEG Technical Program Expanded Abstracts 13, 1139–1142.
Evans, K.F., Scholz, C.H., Engelder, T., 1988. An analysis of horizontal fracture initiation during hydrofrac stress measurements in granite at North-Conway, New-Hampshire. Geophysical Journal-Oxford 93, 251–264.
Ewy, R.T., Cook, N.G.W., 1990. Deformation and fracture around cylindrical openings in rock.1. Observations and analysis of deformations. International Journal of Rock Mechanics and Mining Sciences 27, 387–407.
Exadaktylos, G.E., Liolios, P.A., Stavropoulou, M.C., 2003. A semi-analytical elastic stress-displacement solution for notched circular openings in rocks. International Journal of Solids and Structures 40, 1165–1187.
Fairhurst, C., 1964. Measurement of in situ rock stresses with particular reference to hydraulic fracturing. Felsmechanik und Ingenieurgeologie 2, 129–147.
Fjaer, E., Holt, R., Horsrud, P., Raaen, A., Risnes, R., 2008. Petroleum Related Rock Mechanics, 2nd ed. Elsevier, Amsterdam.
Freund, D., 1992. Ultrasonic compressional and shear velocities in dry clastic rocks as a function of porosity, clay content, and confining pressure. Geophysical Journal International 108, 125–135.
Frignet, B., Sinha, B.K., Winkler, K.W., Kane, M.R., Plona, T.J., 1999. Stress-induced dipole anisotropy: theory, experiment, and field data 1999-RR. SPWLA 40th Annual Logging Symposium,. Soc. Petrophysicists and Well Log Analysts, pp. RR 1–RR 14.
Fuck, R.F., Tsvankin, I., 2009. Analysis of the symmetry of a stressed medium using nonlinear elasticity. Geophysics 74, WB79–WB87.
Galle, E.M., Wilhoit, J.C., 1962. Stresses around a wellbore due to internal pressure and unequal principal geostatic stresses. Society of Petroleum Engineers Journal 2, 145–155.
Germanovich, L.N., Dyskin, A.V., 2000. Fracture mechanisms and instability of openings in compression. International Journal of Rock Mechanics and Mining Sciences 37, 263–284.
Giovanni, B., 1969. Some constitutive equations for rock materials. The 11th U.S. Symposium on Rock Mechanics (USRMS). American Institute of Mining, Metallurgical, and Petroleum Engineers Inc. Permission to Distribute — American Rock Mechanics Association, Berkeley, CA.
Gjonnes, M., Cruz, A., Horsrud, P., Holt, R.M., 1998. Leak-off tests for horizontal stress determination? Journal of Petroleum Science and Engineering 20, 63–71.
Gladwin, M.T., Stacey, F.D., 1974. Ultrasonic pulse velocity as a rock stress sensor. Tectonophysics 21, 39–45.
Golshani, A., Tran-Cong, T., 2009. Energy analysis of hydraulic fracturing. KSCE Journal of Civil Engineering 13, 219–224.
Gorodkov, S., Li, L., Holt, R., 2006. Stress Path during Coring: A Discrete Particle Modelling Approach, In-situ Rock Stress. Taylor & Francis, pp. 541–549.
Gough, D.I., Bell, J.S., 1981. Stress orientations from oil-well fractures in Alberta and Texas. Canadian Journal of Earth Sciences 18, 638–645.
Grasso, M., Pezzino, A., Reuther, C.D., Lanza, R., Miletto, M., 1991. Late Cretaceous and recent tectonic stress orientations recorded by basalt dykes at Capo-Passero (Southeastern Sicily). Tectonophysics 185, 247–259.
Gudmundsson, A., 2006. How local stresses control magma-chamber ruptures, dyke injections, and eruptions in composite volcanoes. Earth-Science Reviews 79, 1–31.
Guenot, A., 1989. Borehole breakouts and stress-fields. International Journal of Rock Mechanics and Mining Sciences 26, 185–195.
Guo, F., Morgenstern, N.R., Scott, J.D., 1993. Interpretation of hydraulic fracturing pressure — a comparison of 8 methods used to identify shut-in pressure. International Journal of Rock Mechanics and Mining Sciences 30, 627–631.
Gurevich, B., Pervukhina, M., Makarynska, D., 2011. An analytic model for the stress-induced anisotropy of dry rocks. Geophysics 76, WA125–WA133.
Haimson, B., 2007. Micromechanisms of borehole instability leading to breakouts in rocks. International Journal of Rock Mechanics and Mining Sciences 44, 157–173.
Haimson, B., 2010a. Reply to discussion by J. Zhang and J-C Roegiers on the paper "Integrating borehole breakout dimensions, strength criteria, and leak-off test results, to constrain the state of stress across the Chelungpu fault, Taiwan" by Bezalel Haimson, Weiren Lin, Haruyuki Oku, Jih-Hao Hung, Sheng-Rong Song, published in Tectonophysics, vol. 482, p. 65–72, 2010. Tectonophysics 492, 299–301.
Haimson, B.C., 2010b. The Effect of Lithology, Inhomogeneity, Topography, and Faults, on In Situ Stress Measurements by Hydraulic Fracturing, and the Importance of Correct Data Interpretation and Independent Evidence in Support of Results. CRC Press-Taylor & Francis Group, Boca Raton.
Haimson, B., Chang, C., 2002. True triaxial strength of the KTB amphibolite under borehole wall conditions and its use to estimate the maximum horizontal in situ stress. Journal of Geophysical Research—Solid Earth 107.
Haimson, B.C., Cornet, F.H., 2003. ISRM suggested methods for rock stress estimation — part 3: hydraulic fracturing (HF) and/or hydraulic testing of pre-existing fractures (HTPF). International Journal of Rock Mechanics and Mining Sciences 40, 1011–1020.
Haimson, B., Fairhurst, C., 1967. Initiation and extension of hydraulic fractures in rocks. Journal of Petroleum Technology 7, 310–318.
Haimson, B., Fairhurst, C., 1969. Hydraulic fracturing in porous-permeable materials. Journal of Petroleum Technology 21, 811-&.
Haimson, B.C., Herrick, C.G., 1986. Borehole breakouts — a new tool for estimating in situ stress? International Symposium on Rock Stress Measurements. Lulea Univ. of Technology, Stockholm, pp. 271–280.
Haimson, B., Lee, M., 1995. Estimating deep in situ stresses from borehole breakouts and core disking — experimental results in granite. Proceedings of the International Workshop on Rock Stress Measurement at Great Depth: 8th International Congress on Rock Mechanics, Tokyo, pp. 19–24.
Haimson, B.C., Tharp, T.M., 1974. Stresses around boreholes in bilinear elastic rock. Society of Petroleum Engineers Journal 14, 145–151.
Haimson, B.C., Lee, M.Y., Song, I., 2003. Shallow hydraulic fracturing measurements in Korea support tectonic and seismic indicators of regional stress. International Journal of Rock Mechanics and Mining Sciences 40, 1243–1256.
Haimson, B., Lin, W.R., Oku, H., Hung, J.H., Song, S.R., 2010. Integrating borehole-breakout dimensions, strength criteria, and leak-off test results, to constrain the state of stress across the Chelungpu fault, Taiwan. Tectonophysics 482, 65–72.
Hakala, M., 1999. Numerical study of the core disk fracturing and interpretation of the in situ state of stress. In: Vouille, G., Berest, P. (Eds.), Ninth International Congress on Rock Mechanics, vols. 1 & 2. AA Balkema Publishers, Leiden, pp. 1149–1153.
Han, T.C., Best, A.I., Sothcott, J., MacGregor, L.M., 2011. Pressure effects on the joint elastic–electrical properties of reservoir sandstones. Geophysical Prospecting 59, 506–517.
Haxby, W.F., Turcotte, D.L., 1976. Stresses induced by addition or removal of overburden and associated thermal effects. Geology 4, 181–184.
Hayashi, K., Haimson, B.C., 1991. Characteristics of shut-in curves in hydraulic fracturing stress measurements and determination of in situ minimum compressive stress. Journal of Geophysical Research—Solid Earth 96, 18311–18321.
Hayashi, K., Kimura, N., Toshiki, K., 2003. Effect of thermal stress on drilling-induced tensile fractures under a variety of far field stress state. In: Sugawara, K., Obara, Y., Sato, A. (Eds.), Rock Stress. AA Balkema Publishers, Leiden, pp. 295–300.
He, T., 2006. P and s wave velocity measurement and pressure sensitivity analysis of AVA response. Physics. University of Alberta, Edmonton, p. 178.
Healy, J.H., Zoback, M.D., 1988. Hydraulic fracturing in situ stress measurements to 2.1 km depth at Cajon Pass, California. Geophysical Research Letters 15, 1005–1008.
Hickman, S.H., Zoback, M.D., 1983. The interpretation of hydraulic fracturing pressure–time data for in-situ stress determination. In: Zoback, M.D., Haimson, B.C. (Eds.), Hydraulic Fracturing Stress Measurements. National Academy Press, Washington, D.C., pp. 44–54.
Hickman, S., Zoback, M., 2004. Stress orientations and magnitudes in the SAFOD pilot hole. Geophysical Research Letters 31.
Hiramatsu, Y., Oka, Y., 1962. Stress around a shaft or level excavated in ground with a three-dimensional stress state. Memoirs of the Faculty of Engineering, Kyoto University Part I 24, 56–76.
Hocking, G., 1976. 3-Dimensional elastic stress distribution around flat end of a cylindrical cavity. International Journal of Rock Mechanics and Mining Sciences 13, 331–337.
Holt, R., Skjaerstein, A., Storemyr, P., 1993. Acoustic anisotropy of deteriorated soapstone from the Nidaros Cathedral, Trondheim, Norway. Canadian Journal of Exploration Geophysics 29, 18–30.
Hubbert, M.K., Willis, D.G., 1957. Mechanics of hydraulic fracturing. Transactions of the American Institute of Mining and Metallurgical Engineers 210, 153–163.
Hurley, N., 2004. Borehole images. In: Asquith, G., Krygowski, D. (Eds.), Basic Well Log Analysis. American Association of Petroleum Geologists, Tulsa, pp. 151–163.
Ito, T., Hayashi, K., 1993. Analysis of crack reopening behavior for hydrofrac stress measurement. International Journal of Rock Mechanics and Mining Sciences 30, 1235–1240.

Ito, T., Kurosawa, K., Hayashi, K., 1998. Stress concentration at the bottom of a borehole and its effect on borehole breakout formation. Rock Mechanics and Rock Engineering 31, 153–168.
Ito, T., Evans, K., Kawai, K., Hayashi, K., 1999. Hydraulic fracture reopening pressure and the estimation of maximum horizontal stress. International Journal of Rock Mechanics and Mining Sciences 36, 811–825.
Ito, T., Kato, H., Tanaka, H., 2006. Innovative Concept of Hydrofracturing for Deep Stress Measurement, In-situ Rock Stress. Taylor & Francis, pp. 53–60.
Jaeger, J.C., Cook, N.G.W., 1963. Pinching-off and disking of rocks. Journal of Geophysical Research 68, 1759-&.
Jaeger, J., Cook, N., Zimmerman, R., 2007. Fundamentals of Rock Mechanics. Wiley-Blackwell, New York.
Johnson, P.A., Rasolofosaon, P.N.J., 1996. Nonlinear elasticity and stress-induced anisotropy in rock. Journal of Geophysical Research 101, 3113–3124.
Kaga, N., Matsuki, K., Sakaguchi, K., 2003. The in situ stress states associated with core discing estimated by analysis of principal tensile stress. International Journal of Rock Mechanics and Mining Sciences 40, 653–665.
Kaiser, J., 1950. Untersuchung über das auftreten von geräuschen beim zugversuch. Fakultät für Maschinenwesen und Elektrotechnik der Technischen Universität München (TUM), p. 152.
Kanamori, H., Brodsky, E.E., 2004. The physics of earthquakes. Reports on Progress in Physics 67, 1429–1496.
Kang, S.S., Ishiguro, Y., Obara, Y., 2006. Evaluation of core disking rock stress and tensile strength via the compact conical-ended borehole overcoring technique. International Journal of Rock Mechanics and Mining Sciences 43, 1226–1240.
Katsman, R., Haimson, B.C., 2011. Modelling partially-emptied compaction bands induced by borehole drilling. Journal of Structural Geology 33, 690–697.
Katsman, R., Aharonov, E., Haimson, B.C., 2009. Compaction bands induced by borehole drilling. Acta Geotechnica 4, 151–162.
Kehle, R.O., 1964. Determination of tectonic stresses through analysis of hydraulic well fracturing. Journal of Geophysical Research 69, 259-&.
Kirsch, G., 1898. Die theorie der elastizitat und die bedurfnisse der festigkeitslehre. Zeitschrift der Vereins deutscher Ingenieure 42, 797–807.
Klee, G., Rummel, F., 1993. Hydrofrac stress data for the European HDR research-project test site Soultz-Sous-Forets. International Journal of Rock Mechanics and Mining Sciences 30, 973–976.
Klee, G., Bunger, A., Meyer, G., Rummel, F., Shen, B., 2011. In situ stresses in borehole Blanche-1/South Australia derived from breakouts, core discing and hydraulic fracturing to 2 km depth. Rock Mechanics and Rock Engineering 44, 531–540.
Kulander, B.R.D., Stuart, L., Billy, J., 1990. Fractured Core Analysis; Interpretation, Logging, and Use of Natural and Induced Fractures in Core. American Association of Petroleum Geologists, Tulsa.
Leeman, E., Hayes, D., 1966. A technique for determining the complete state of stress in rock using a single borehole. Proceedings 1st Congress International Society of Rock Mechanics, Lisbon, pp. 17–24.
Lei, T., Sinha, B.K., Sanders, M., 2012. Estimation of horizontal stress magnitudes and stress coefficients of velocities using borehole sonic data. Geophysics 77, WA181–WA196.
Leite, M.H., Boivin, V., Corthesy, R., 2010. Stress calculation methods for overcoring techniques in heterogeneous rocks. International Journal of Rock Mechanics and Mining Sciences 47, 1180–1192.
Li, L., Aubertin, M., 2009. An elastoplastic evaluation of the stress state around cylindrical openings based on a closed multiaxial yield surface. International Journal for Numerical and Analytical Methods in Geomechanics 33, 193–213.
Li, C., Nordlund, E., 1993. Experimental-verification of the Kaiser effect in rocks. Rock Mechanics and Rock Engineering 26, 333–351.
Li, Y.Y., Schmitt, D.R., 1997a. Effects of Poisson's ratio and core stub length on bottomhole stress concentrations. International Journal of Rock Mechanics and Mining Sciences 34, 761–773.
Li, Y.Y., Schmitt, D.R., 1997b. Well-bore bottom stress concentration and induced core fractures. AAPG Bulletin—American Association of Petroleum Geologists 81, 1909–1925.
Li, Y.Y., Schmitt, D.R., 1998. Drilling-induced core fractures and in situ stress. Journal of Geophysical Research—Solid Earth 103, 5225–5239.
Li, S.C., Wang, M.B., 2008. Elastic analysis of stress-displacement field for a lined circular tunnel at great depth due to ground loads and internal pressure. Tunnelling and Underground Space Technology 23, 609–617.
Lim, S., Martin, C., 2010. Core disking and its relationship with stress magnitude for Lac du Bonnet granite. International Journal of Rock Mechanics and Mining Sciences 47, 254–264.
Lim, S., Martin, C., Christiansson, R., 2006. Estimating in-situ stress magnitudes from core disking. In: Lu, M., Li, C., Kjorholt, H., Dahle, H. (Eds.), International Symposium on In-situ Rock Stress. Taylor & Francis, Trondheim, pp. 159–166.
Lin, P., Tommy, G.R., 1994. A new method for direct measurement of in-situ stress directions and formation rock properties. SPE Journal of Petroleum Technology 46, 249–254.
Lin, W.R., Kwasniewski, M., Imamura, T., Matsuki, K., 2006. Determination of three-dimensional in situ stresses from anelastic strain recovery measurement of cores at great depth. Tectonophysics 426, 221–238.
Lin, W.R., Yeh, E.C., Hung, J.H., Haimson, B., Hirono, T., 2010. Localized rotation of principal stress around faults and fractures determined from borehole breakouts in hole B of the Taiwan Chelungpu-Fault Drilling Project (TCDP). Tectonophysics 482, 82–91.
Lucier, A.M., Zoback, M.D., Heesakkers, V., Reches, Z., Murphy, S.K., 2009. Constraining the far-field in situ stress state near a deep South African gold mine. International Journal of Rock Mechanics and Mining Sciences 46, 555–567.
Lyakhovsky, V., Reches, Z., Weinberger, R., Scott, T.E., 1997. Non-linear elastic behaviour of damaged rocks. Geophysical Journal International 130, 157–166.
Mahtab, M.A., Goodman, R.E., 1968. Stresses around Wellbores in Nonlinear Rock, p. 8.
Majmudar, T.S., Behringer, R.P., 2005. Contact force measurements and stress-induced anisotropy in granular materials. Nature 435, 1079–1082.
Makse, H.A., Gland, N., Johnson, D.L., Schwartz, L.M., 1999. Why effective medium theory fails in granular materials. Physical Review Letters 83, 5070–5073.
Manthei, G., Eisenblatter, J., Kamlot, P., 2003. Stress measurements in salt mines using a special hydraulic fracturing borehole tool. In: Natau, O., Fecker, E., Pimentel, E. (Eds.), Geotechnical Measurements and Modelling, pp. 355–360.
Martin, C.D., Read, R.S., Martino, J.B., 1997. Observations of brittle failure around a circular test tunnel. International Journal of Rock Mechanics and Mining Sciences 34, 1065–1073.
Mastin, L., 1988. Effect of borehole deviation on breakout orientations. Journal of Geophysical Research—Solid Earth and Planets 93, 9187–9195.
Matsuki, K., 2008. Anelastic strain recovery compliance of rocks and its application to in situ stress measurement. International Journal of Rock Mechanics and Mining Sciences 45, 952–965.
Matsuki, K., Takeuchi, K., 1993. 3-Dimensional in-situ stress determination by anelastic strain recovery of a rock core. International Journal of Rock Mechanics and Mining Sciences 30, 1019–1022.
Matsuki, K., Kaga, N., Yokoyama, T., Tsuda, N., 2003. Determination of three-dimensional directions of in situ stress from core discing. In: Sugawara, K., Obara, Y., Sato, A. (Eds.), Rock Stress, pp. 237–243.
Matsuki, K., Kaga, N., Yokoyama, T., Tsuda, N., 2004. Determination of three dimensional in situ stress from core discing based on analysis of principal tensile stress. International Journal of Rock Mechanics and Mining Sciences 41, 1167–1190.
McCutchen, W.R., 1982. Some elements of a theory for in situ stress. International Journal of Rock Mechanics and Mining Sciences 19, 201–203.
Meglis, I.L., Greenfield, R.J., Engelder, T., Graham, E.K., 1996. Pressure dependence of velocity and attenuation and its relationship to crack closure in crystalline rocks. Journal of Geophysical Research—Solid Earth 101, 17523–17533.
Meyer, B., Jacot, H., 2001. Impact of stress-dependent Young's moduli on hydraulic fracture modeling, DC Rocks 2001. The 38th U.S. Symposium on Rock Mechanics (USRMS). Swets & Zeitlinger Lisse, Permission to Distribute - American Rock Mechanics Association, Washington D.C.
Mitaim, S., Detournay, E., 2004. Damage around a cylindrical opening in a brittle rock mass. International Journal of Rock Mechanics and Mining Sciences 41, 1447–1457.
Mollema, P.N., Antonellini, M.A., 1996. Compaction bands: a structural analog for anti-mode I cracks in aeolian sandstone. Tectonophysics 267, 209–228.
Moore, J.C., Chang, C., McNeill, L., Thu, M.K., Yamada, Y., Huftile, G., 2011. Growth of borehole breakouts with time after drilling: implications for state of stress, NanTroSEIZE transect, SW Japan. Geochemistry, Geophysics, Geosystems 12.
Morin, R.H., 1990. Information on stress conditions in the oceanic-crust from oval fractures in a deep borehole. Geophysical Research Letters 17, 1311–1314.
Morin, R.H., Wilkens, R.H., 2005. Structure and stress state of Hawaiian island basalts penetrated by the Hawaii Scientific Drilling Project deep core hole. Journal of Geophysical Research—Solid Earth 110.
Murdoch, L.C., 1995. Forms of hydraulic fractures created during a field-test in overconsolidated glacial drift. The Quarterly Journal of Engineering Geology 28, 23–35.
Murray, D., Plona, T.J., Valero, H.P., 2004. Case study of borehole sonic dispersion curve analysis paper BB. SPWLA 45th Annual Logging Symposium. Society of Petrophysicists and Well Log Analysts, Noordwijk, pp. BB 1–BB 14.
Nawrocki, P., 2010. Critical wellbore pressures using different rock failure criteria. ISRM International Symposium — 6th Asian Rock Mechanics Symposium. Central Board of Irrigation and Power (CBIP) and International Society for Rock Mechanics (ISRM), New Delhi, India.
Nelson, E.J., Meyer, J.J., Hillis, R.R., Mildren, S.D., 2005. Transverse drilling-induced tensile fractures in the West Tuna area, Gippsland Basin, Australia: implications for the in situ stress regime. International Journal of Rock Mechanics and Mining Sciences 42, 361–371.
Nelson, E.J., Chipperfield, S.T., Hillis, R.R., Gilbert, J., McGowen, J., Mildren, S.D., 2007. The relationship between closure pressures from fluid injection tests and the minimum principal stress in strong rocks. International Journal of Rock Mechanics and Mining Sciences 44, 787–801.
Nur, A., Simmons, G., 1969. Stress-induced velocity anisotropy in rock — an experimental study. Journal of Geophysical Research 74, 6667-&.
Obert, L., Stephenson, D., 1965. Stress conditions under which core disking occurs. Society of Mechanical Engineers Transactions 323, 227–235.
Ode, H., 1957. Mechanical analysis of the dike pattern of the Spanish Peaks area, Colorado. Geological Society of America Bulletin 68, 567–575.
Okabe, T., Hayashi, K., Shinohara, N., Takasugi, S., 1998. Inversion of drilling-induced tensile fracture data obtained from a single inclined borehole. International Journal of Rock Mechanics and Mining Sciences 35, 747–758.
Ou, Z.Y., Wang, G.F., Wang, T.J., 2009. An analytical solution for the elastic fields near spheroidal nano-inclusions. Acta Mechanica Sinica 25, 821–830.
Paillet, F.L., Kim, K., 1987. Character and distribution of borehole breakouts and their relationship to in situ stresses in deep Columbia River basalts. Journal of Geophysical Research—Solid Earth and Planets 92, 6223–6234.
Papanastasiou, P., Durban, D., 1997. Elastoplastic analysis of cylindrical cavity problems in geomaterials. International Journal for Numerical and Analytical Methods in Geomechanics 21, 133–149.
Pascal, C., Roberts, D., Gabrielsen, R.H., 2010. Tectonic significance of present-day stress relief phenomena in formerly glaciated regions. Journal of the Geological Society 167, 363–371.
Paulsen, T., Wilson, T., 2007. Elongate summit calderas as neogene paleostress indicators in Antarctica. Short Research Paper 072, Online Proceedings of the 10th ISAES, USGS Open File Report 2007–1047.

Paulsen, T.S., Wilson, T.J., 2010. New criteria for systematic mapping and reliability assessment of monogenetic volcanic vent alignments and elongate volcanic vents for crustal stress analyses. Tectonophysics 482, 16–28.
Payan, C., Garnier, V., Moysan, J., Johnson, P.A., 2009. Determination of third order elastic constants in a complex solid applying coda wave interferometry. Applied Physics Letters 94.
Peska, P., Zoback, M.D., 1995. Compressive and tensile failure of inclined well bores and determination of in-situ stress and rock strength. Journal of Geophysical Research—Solid Earth 100, 12791–12811.
Pilkey, W., Pilkey, D., Peterson, R., 2008. Peterson's Stress Concentration Factors, 3rd ed. Wiley, New York.
Pistre, V., Kinoshita, T., Endo, T., Schilling, J., Pabon, J., Sinha, B.K., Plona, T., Ikegami, T., Johnson, D.L., 2005. A modular wireline sonic tool for measurements of 3d (azimuthal, radial, and axial) formation acoustic properties. SPWLA 46th Annual Logging Symposium, New Orleans, pp. P1–P13.
Plona, T.J., Winkler, K.W., Sinha, B.K., D'Angelo, R., 1998. Measurement of stress direction and mechanical damage around stressed boreholes using dipole and microsonic techniques. SPE/ISRM Rock Mechanics in Petroleum Engineering. Society of Petroleum Engineers Inc., Trondheim, Norway. Copyright 1998.
Plona, T.J., Kane, M.R., Sinha, B., Walsh, J., 2002. Evaluating stress-induced anisotropy and mechanical damage from cross-dipole sonic data using dispersion analysis SPE/ISRM 78233. SPE/ISRM Rock Mechanics Conference. Soc. Petr. Eng., Irving, p. 6.
Plumb, R.A., Hickman, S.H., 1985. Stress-induced borehole elongation — a comparison between the 4-arm dipmeter and the borehole televiewer in the auburn geothermal well. Journal of Geophysical Research—Solid Earth and Planets 90, 5513–5521.
Polymetra, G., 2012. Hydraulic Fracturing Tests.
Pook, L.P., 2010. Five decades of crack path research. Engineering Fracture Mechanics 77, 1619–1630.
Pöppelreiter, M., Garcia-Carballido, C., Kraaijveld, M., 2010. Borehole image log technology: application across the exploration and production cycle. In: Pöppelreiter, M., Garcia-Carballido, C., Kraaijveld, M. (Eds.), Dipmeter and Borehole Image Log Technology. American Association of Petroleum Geologists, Tulsa, pp. 1–13.
Prikryl, R., Klima, K., Lokajicek, T., Pros, Z., 2005. Non-linearity in multidirectional p-wave velocity; confining pressure behaviour based on real 3d laboratory measurements, and its mathematical approximation. In: Harvey, P.K., Brewer, T.S., Pezard, P.A., Petrov, V.A. (Eds.), Petrophysical Properties of Crystalline Rocks. Geological Society of London, pp. 323–334.
Raaen, A.M., Horsrud, P., Kjorholt, H., Okland, D., 2006. Improved routine estimation of the minimum horizontal stress component from extended leak-off tests. International Journal of Rock Mechanics and Mining Sciences 43, 37–48.
Raleigh, C.B., Healy, J.H., Bredehoeft, J.D., 1972. Faulting and crustal stress at Rangely, Colorado. In: Heard, H.C. (Ed.), Flow and Fracture of Rocks. American Geophysical Union, Washington, DC, pp. 275–284.
Rathore, J.S., Fjaer, E., Holt, R.M., Renlie, L., 1995. P-wave and s-wave anisotropy of a synthetic sandstone with controlled crack geometry. Geophysical Prospecting 43, 711–728.
Ratigan, J.L., 1992. The use of the fracture reopening pressure in hydraulic fracturing stress measurements. Rock Mechanics and Rock Engineering 25, 225–236.
Reuschlé, T., Gbaguidi Haore, S., Darot, M., 2006. The effect of heating on the microstructural evolution of La Peyratte granite deduced from acoustic velocity measurements. Earth and Planetary Science Letters 243, 692–700.
Rice, J.R., Cleary, M.P., 1976. Some basic stress diffusion solutions for fluid-saturated elastic porous-media with compressible constituents. Reviews of Geophysics 14, 227–241.
Ritchie, R.H., Sakakura, A.Y., 1956. Asymptotic expansions of solutions of the heat conduction equation in internally bounded cylindrical geometry. Journal of Applied Physics 27, 1453–1459.
Roshan, H., Rahman, S., 2011. Analysis of pore pressure and stress distribution around a wellbore drilled in chemically active elastoplastic formations. Rock Mechanics and Rock Engineering 1–12.
Ruch, J., Walter, T.R., 2010. Relationship between the inSAR-measured uplift, the structural framework, and the present-day stress field at Lazufre volcanic area, Central Andes. Tectonophysics 492, 133–140.
Rumzan, I., Schmitt, D.R., 2001. The influence of well bore fluid pressure on drilling penetration rates and stress dependent strength. In: Elsworth, D., Tinucci, J.P., Heasley, K.A. (Eds.), Rock Mechanics in the National Interest, vols. 1 and 2. AA Balkema Publishers, Leiden, pp. 911–917.
Rutqvist, J., Tsang, C.F., Stephansson, O., 2000. Uncertainty in the maximum principal stress estimated from hydraulic fracturing measurements due to the presence of the induced fracture. International Journal of Rock Mechanics and Mining Sciences 37, 107–120.
Saner, S., Amabeoku, M., Kissami, M., 1996. Formation resistivity response to loading and unloading confining pressure. Journal of Petroleum Science and Engineering 16, 169–179.
Santarelli, F.J., Brown, E.T., Maury, V., 1986. Analysis of borehole stresses using pressure-dependent, linear elasticity. International Journal of Rock Mechanics and Mining Sciences & Geomechanics Abstracts 23, 445–449.
Savage, W.Z., Morin, R.H., 2002. Topographic stress perturbations in Southern Davis Mountains, West Texas — 1. Polarity reversal of principal stresses. Journal of Geophysical Research—Solid Earth 107.
Sayers, C.M., 2007. Effects of borehole stress concentration on elastic wave velocities in sandstones. International Journal of Rock Mechanics and Mining Sciences 44, 1045–1052.
Sayers, C.M., 2010. Geophysics under Stress: Geomechanical Applications of Seismic and Borehole Acoustic Waves. Society of Exploration Geophysicists and the European Association of Geoscientists and Engineers.
Sayers, C.M., Vanmunster, J.G., King, M.S., 1990. Stress-induced ultrasonic anisotropy in Berea sandstone. International Journal of Rock Mechanics and Mining Sciences 27, 429–436.
Scheidegger, A.E., 1960. On the connection between tectonic stresses and well fracturing data. Pure and Applied Geophysics 46, 66–76.
Schmitt, D.R., 1993. Fracture statistics derived from digital ultrasonic televiewer logging. Journal of Canadian Petroleum Technology 32, 34–43.
Schmitt, D.R., Zoback, M.D., 1992. Diminished pore pressure in low-porosity crystalline rock under tensional failure — apparent strengthening by dilatancy. Journal of Geophysical Research—Solid Earth 97, 273–288.
Schmitt, D.R., Zoback, M.D., 1993. Infiltration effects in the tensile rupture of thin-walled cylinders of glass and granite — implications for the hydraulic fracturing breakdown equation. International Journal of Rock Mechanics and Mining Sciences 30, 289–303.
Schmitt, D.R., Smither, C., Ahrens, T.J., 1989. In situ holographic elastic-moduli measurements from boreholes. Geophysics 54, 468–477.
Schmitt, D.R., Diallo, M.S., Weichman, F., 2006. Quantitative determination of stress by inversion of speckle interferometer fringe patterns: experimental laboratory tests. Geophysical Journal International 167, 1425–1438.
Schmitt, D.R., Wilson, T., Jarrard, R., Paulsen, T., Pierdominici, S., Wonik, T., Handwerger, D., 2011. ANDRILL experiences with a wireline hydraulic fracturing system for minifrac stress measurements in indurated sediments. CSPG–CSEG–CWLS Joint Convention. CSPG, Calgary. p. Electronic 4.
Schmitt, D.R., Wilson, T.J., Jarrard, R.D., Paulsen, T., Pierdominici, S., Grelle, T., Handwerger, D., Wonik, T., 2012. Hydraulic fracturing stress determinations in the ANDRILL South Mcmurdo sound drill hole, Antarctica. 46th U.S. Rock Mechanics Symposium. American Rock Mechanics Symposium, Chicago, p. 8. CDROM.
Schultz, R.A., 2009. Scaling and paleodepth of compaction bands, Nevada and Utah. Journal of Geophysical Research—Solid Earth 114.
Sharma, M.S.R., O'Regan, M., Baxter, C.D.P., Moran, K., Vaziri, H., Narayanasamy, R., 2010. Empirical relationship between strength and geophysical properties for weakly cemented formations. Journal of Petroleum Science and Engineering 72, 134–142.
Sheorey, P.R., 1994. A theory for in-situ stresses in isotropic and transversely isotropic rock. International Journal of Rock Mechanics and Mining Sciences & Geomechanics Abstracts 31, 23–34.
Sheorey, P.R., Mohan, G.M., Sinha, A., 2001. Influence of elastic constants on the horizontal in situ stress. International Journal of Rock Mechanics and Mining Sciences 38, 1211–1216.
Simon, R., Labrie, D., 2012. Using borehole breakouts to estimate in situ stresses at depth. 46th US Rock Mechanics/Geomechanics Symposium. American Rock Mechanics Association, Chicago, p. 8.
Sinha, B.K., Kostek, S., 1996. Stress-induced azimuthal anisotropy in borehole flexural waves. Geophysics 61, 1899–1907.
Sinha, B.K., Norris, A.N., Chang, S.K., 1994. Borehole flexural modes in anisotropic formations. Geophysics 59, 1037–1052.
Sinha, B.K., Wang, J., Kisra, S., Li, J., Pistre, V., Bratton, T., Sanders, M., Jun, C., 2008. Estimation of formation stresses using borehole sonic data. SPWLA 49th Annual Logging Symposium, Edinburgh, pp. F1–F16.
Song, I., Haimson, B., 1999. Core disking in Westerly granite and its potential use for in situ stress estimation. In: Amadei, B., Kranz, R., Scott, G. (Eds.), Rock Mechanics for Industry: Proceedings of the 37th U.S. Rock Mechanics Symposium. Balkema, Vail, CO, pp. 1172–1180.
Stanchits, S., Fortin, J., Gueguen, Y., Dresen, G., 2009. Initiation and propagation of compaction bands in dry and wet Bentheim sandstone. Pure and Applied Geophysics 166, 843–868.
Stephannson, O., 1983. Rock stress measurements by sleeve fracturing. 5th Congress of the International Society of Rock Mechanics. Balkema, Rotterdam, Melbourne, pp. F129–F137.
Stephens, G., Voight, B., 1982. Hydraulic fracturing theory for conditions of thermal-stress. International Journal of Rock Mechanics and Mining Sciences 19, 279–284.
Stock, J.M., Healy, J.H., Hickman, S.H., Zoback, M.D., 1985. Hydraulic fracturing stress measurements at Yucca Mountain, Nevada, and relationship to the regional stress-field. Journal of Geophysical Research—Solid Earth and Planets 90, 8691–8706.
Sugawara, K., Kemeoka, Y., Saito, T., Oka, Y., Hiramatsu, Y., 1978. A study on core disking of rock. Journal of Japanese Association of Mining 94, 19–25.
Tang, X.M., Cheng, A., 2004. Quantitative Borehole Acoustic Methods. Elsevier, Amsterdam.
Tembe, S., Baud, P., Wong, T.F., 2008. Stress conditions for the propagation of discrete compaction bands in porous sandstone. Journal of Geophysical Research—Solid Earth 113.
Teufel, L.W., Hart, C.M., Sattler, A.R., Clark, J.A., 1984. Determination of hydraulic fracture azimuth by geophysical, geological, and oriented-core methods at the Multiwell Experiment Site, Rifle, CO. SPE Annual Technical Conference and Exhibition. Soc. Petroleum Engineers, Houston, Texas.
Thiercelin, M.J., Plumb, R.A., Desroches, J., Bixenman, P.W., Jonas, J.K., Davie, W.A.R., 1996. A new wireline tool for in-situ stress measurements. SPE Formation Evaluation, 11.
Thorsen, K., 2011. In situ stress estimation using borehole failures — even for inclined stress tensor. Journal of Petroleum Science and Engineering 79, 86–100.
Timoshenko, S., Goodier, J., 1970. Theory of Elasticity, 3rd ed. McGraw-Hill, New York.
Tokar, G., 1990. Experimental-analysis of the elastoplastic zone surrounding a borehole in a specimen of rock-like material under multiaxial pressure. Engineering Fracture Mechanics 35, 879-&.
Valley, B., Evans, K.F., 2009. Stress orientation to 5 km depth in the basement below Basel (Switzerland) from borehole failure analysis. Swiss Journal of Geosciences 102, 467–480.

Venet, V., 1993. Contribution to the optimizing of core drilling by modeling the initiation of discing. Revue De L Institut Francais Du Petrole 48, 15–42.
Venet, V., Henry, J.P., Santarelli, F.J., Maury, V., 1990. Modelisation du discage pour l'estimation des contraintes in situ a grande profondeur. In: Maury, V., Formaintraux, D. (Eds.), Rock at Great Depth: Rock Mechanics and Rock Physics at Great Depth. Balkema, Pau, pp. 1551–1557.
Vernik, L., Zoback, M.D., 1992. Estimation of maximum horizontal principal stress magnitude from stress-induced well bore breakouts in the Cajon Pass scientific-research borehole. Journal of Geophysical Research 97, 5109–5119.
Vilhelm, J., Rudajev, V., Zivor, R., Lokajicek, T., Pros, Z., 2010. Influence of crack distribution of rocks on p-wave velocity anisotropy — a laboratory and field scale study. Geophysical Prospecting 58, 1099–1110.
Walsh, J.B., 1965. Effect of cracks on compressibility of rock. Journal of Geophysical Research 70, 381–389.
Wang, Y., Wong, T.F., 1987. Finite-element analysis of 2 overcoring techniques for in situ stress measurement. International Journal of Rock Mechanics and Mining Sciences 24, 41–52.
Warpinski, N.R., 1989. Altered-stress fracturing. Journal of Petroleum Technology 41, 990–997.
Warpinski, N.R., Teufel, L.W., 1991. In situ stress measurements at Rainier Mesa, Nevada test site — influence of topography and lithology on the stress state in tuff. International Journal of Rock Mechanics and Mining Sciences 28, 143–161.
Warren, W.E., 1981. Packer-induced stresses during hydraulic well fracturing. Journal of Energy Resources Technology—Transactions of the ASME 103, 336–343.
Warren, W.E., Smith, C.W., 1985. In situ stress estimates from hydraulic fracturing and direct observation of crack orientation. Journal of Geophysical Research—Solid Earth and Planets 90, 6829–6839.
Wawersik, W.R., Stone, C.M., 1989. A characterization of pressure records in inelastic rock demonstrated by hydraulic fracturing measurements in salt. International Journal of Rock Mechanics and Mining Sciences 26, 613–627.
Williams, J.H., Johnson, C.D., 2004. Acoustic and optical borehole-wall imaging for fractured-rock aquifer studies. Journal of Applied Geophysics 55, 151–159.
Wilson, T., Paulsen, T., 2000. Brittle deformation patterns of crp-2/2a, Victoria Land Basin, Antarctica. Terra Antartica 7, 287–298.
Winkler, K.W., 1996. Azimuthal velocity variations caused by borehole stress concentrations. Journal of Geophysical Research—Solid Earth 101, 8615–8621.
Winkler, K.W., D'Angelo, R., 2006. Ultrasonic borehole velocity imaging. Geophysics 71, F25–F30.
Winkler, K.W., Sinha, B.K., Plona, T.J., 1998. Effects of borehole stress concentrations on dipole anisotropy measurements. Geophysics 63, 11–17.
Wiprut, D., Zoback, M., 2000. Constraining the stress tensor in the Visund field, Norwegian North Sea: application to wellbore stability and sand production. International Journal of Rock Mechanics and Mining Sciences 37, 317–336.
Wolter, K.E., Berckhemer, H., 1989. Time-dependent strain recovery of cores from the KTB — deep drill hole. Rock Mechanics and Rock Engineering 22, 273–287.
Wolter, K.E., Berckhemer, H., 1990. Estimation of in situ stresses by evaluation of time-dependent strain recovery of KTB drill cores. Tectonophysics 178, 255–257.
Wu, B., King, M.S., Hudson, J.A., 1991. Stress-induced ultrasonic wave velocity anisotropy in a sandstone. International Journal of Rock Mechanics and Mining Sciences 28, 101–107.
Wu, R., Germanovich, L.N., Van Dyke, P.E., Lowell, R.P., 2007. Thermal technique for controlling hydraulic fractures. Journal of Geophysical Research—Solid Earth 112.
Yamamoto, K., 2009. A theory of rock core-based methods for in-situ stress measurement. Earth Planets Space 61, 1143–1161.
Yamashita, F., Mizoguchi, K., Fukuyama, E., Omura, K., 2010. Reexamination of the present stress state of the Atera fault system, Central Japan, based on the calibrated crustal stress data of hydraulic fracturing tests obtained by measuring the tensile strength of rocks. Journal of Geophysical Research—Solid Earth 115.
Yin, Z.M., Ranalli, G., 1992. Critical stress difference, fault orientation and slip direction in anisotropic rocks under non-Andersonian stress systems. Journal of Structural Geology 14, 237–244.
Zang, A., Stephannson, O., 2010. Stress Field in the Earth's Crust. Springer, Amsterdam.
Zemanek, J., Angona, F.A., Williams, D.M., Caldwell, R.L., 1984. Continuous acoustic shear wave logging. SPWLA 25th Annual Logging Symposium, pp. U1–U14.
Zhang, L., 2011. Three-dimensional numerical models of drilling induced core fractures. Physics. University of Alberta, Edmonton, p. 276.
Zhang, J.C., Roegiers, J.C., 2010. Discussion on "Integrating borehole-breakout dimensions, strength criteria, and leak-off test results, to constrain the state of stress across the Chelungpu fault, Taiwan". Tectonophysics 492, 295–298.
Zhang, C.G., Zhao, J.H., Zhang, Q.H., Hu, X.D., 2012. A new closed-form solution for circular openings modeled by the unified strength theory and radius-dependent Young's modulus. Computers and Geotechnics 42, 118–128.
Zheng, Z., 2000. Seismic anisotropy due to stress-induced cracks. International Journal of Rock Mechanics and Mining Sciences 37, 39–49.
Zheng, Z.Q., Kemeny, J., Cook, N.G.W., 1989. Analysis of borehole breakouts. Journal of Geophysical Research—Solid Earth and Planets 94, 7171–7182.
Zhou, X.P., Bao, X.R., Yu, M.H., Xie, Q., 2010. Triaxial stress state of cylindrical openings for rocks modeled by elastoplasticity and strength criterion. Theoretical and Applied Fracture Mechanics 53, 65–73.
Zisman, W.A., 1933. Compressibility and anisotropy of rocks at and near the earth's surface. Proceedings of the National Academy of Sciences of the United States of America 19, 666–679.
Zoback, M.D., 2007. Reservoir Geomechanics. Cambridge University Press, Cambridge.
Zoback, M.D., Moos, D., Mastin, L., Anderson, R.N., 1985. Well bore breakouts and in situ stress. Journal of Geophysical Research—Solid Earth and Planets 90, 5523–5530.
Zoback, M.L., Zoback, M.D., Adams, J., Assumpcao, M., Bell, S., Bergman, E.A., Blumling, P., Brereton, N.R., Denham, D., Ding, J., Fuchs, K., Gay, N., Gregersen, S., Gupta, H.K., Gvishiani, A., Jacob, K., Klein, R., Knoll, P., Magee, M., Mercier, J.L., Muller, B.C., Paquin, C., Rajendran, K., Stephansson, O., Suarez, G., Suter, M., Udias, A., Xu, Z.H., Zhizhin, M., 1989. Global patterns of tectonic stress. Nature 341, 291–298.
Zoback, M.D., Barton, C.A., Brudy, M., Castillo, D.A., Finkbeiner, T., Grollimund, B.R., Moos, D.B., Peska, P., Ward, C.D., Wiprut, D.J., 2003. Determination of stress orientation and magnitude in deep wells. International Journal of Rock Mechanics and Mining Sciences 40, 1049–1076.